FERMILAB-PUB-11-172-CD

Coupling impedance and wake functions for laminated structures with an application to the Fermilab Booster

Alexandru Macridin, Panagiotis Spentzouris, James Amundson
Fermilab, P.O. Box 500, Batavia, Illinois 60510, USA

Linda Spentzouris, Daniel McCarron
Illinois Institute of Technology, Chicago, Illinois, USA

We calculate the impedance and the wake functions for laminated structures with parallel-plane and circular geometries. We critically examine the approximations used in the literature for the coupling impedance in laminated chambers and find that most of them are not justified because the wall surface impedance is large. A comparison between the flat and the circular geometry impedance is presented. We apply our calculation in a state-of-the-art beam dynamics simulation of the Fermilab Booster which includes not only wake field effects, but also non-linear optics and three-dimensional space charge. We find good agreement between our calculation of the coherent tune shift at injection energy and recent experimental measurements.

I. INTRODUCTION

Wake fields are an important component of beam dynamics in high-intensity accelerators, being a potential cause for losses and instabilities. While there is satisfactory understanding of wake fields in metallic chambers with smooth geometries, the attempts to describe the impedance effect in structures with laminations are not in very good agreement with experimental measurements. Magnetic elements for guiding and focusing beams are often constructed from stacks of iron laminations alternating with the layers of epoxy holding them together. In the absence of beam pipe the presence of laminations produces large wake effects. Due to the strong demand for increasing intensity in machines with laminated chambers, such as the Fermilab Booster synchrotron, theoretical investigation of wake effects in the presence of laminations is of paramount importance.

In addition to improved calculations of the effects of wake fields, realistic simulations which consider the interplay between wake fields and other effects in accelerators must be employed to accurately describe beam dynamics and and to compare with measurements. While most of the analytical investigations of wake effects have been done in the frequency domain and require an impedance function over some finite frequency range, beam simulation algorithms require point-charge wake functions in the time-and-space domain. The impedance calculation is in general much easier; the wake fields are related to the impedance via a Fourier transform. However, this method requires knowledge of the impedance over a large frequency domain as well as the asymptotic behavior at both small and large frequencies.

In this paper we calculate the impedance and the wake functions for laminated structures with parallel-plane and circular geometries. First the coupling impedance is derived as a function of the wall surface impedance. Then the surface impedance is calculated by solving the Maxwell equations inside the lamination and the crack regions. A critical analysis of the resistive-wall impedance for metallic chambers and the approximations involved in its derivations is also presented.

The Fermilab Booster is a good example of a machine where the beam is exposed to laminations. It is currently running with beam intensities roughly twice its design value. Direct measurements using a stretched wire between the gradient magnets ends indicate a large longitudinal coupling impedance [3]. The coherent tune shift, which shows horizontal tune increase and vertical tune decrease, presents strong evidence for large transverse wakes [4]. Since the effect on the transverse tunes is specific to geometries without circular symmetries [5], these measurements also stress the importance of choosing the right chamber geometry for any calculation which address the wakes in the Booster magnets.

There are several calculations of the impedance due to laminated structures with applications for the Fermilab Booster [6–9]. Most of them [6–8] address only circular geometry, which is a poor approximation for the Booster magnets. Moreover, the resistive-wall specific relation they use to connect the wall surface impedance to the coupling impedance is not valid for structures with large surface impedance and flat chambers such as the laminated magnets in the Booster. Even for the circular geometry they address only the longitudinal impedance for uniform round beams, i.e. only the $m = 0$ angular channel. However, since the commonly encountered relation valid for metallic pipes which connects the longitudinal impedance $Z_0^{||}$ (in the $m = 0$ channel) and the transverse impedance $Z_1^{\perp}$ (in the $m = 1$ channel) is not valid for the laminated structures, calculations in the $m = 1$ channel are necessary to address the transverse impedance. K. Y. Ng [9] addresses both the parallel-plane geometry, which is close to the real geometry of the Booster magnets [10], and the transverse impedance. However, for the sake of simplicity, he assumes a beam

Operated by Fermi Research Alliance, LLC under Contract No. DE-AC02-07CH11359 with the United States Department of Energy

which extends to infinity in the horizontal direction. While this approximation works for metallic pipes, it produces wakes which are too large for laminated chambers. When applied to the Fermilab Booster magnets, we find that our derivation of the longitudinal impedance gives a better agreement with the one measured by Crisp and Fellenz [3] than do the previous calculations.

We employ the Synergia code to run realistic beam simulations which include wake interactions specific to laminated structures. Synergia is an extensible beam dynamics framework developed at Fermilab [1, 2] which incorporates a large collection of physical models, specialized modules and numerical libraries. Synergia simulates complex beam dynamics, employing high order maps to describe single particle propagation through accelerators and considers collective effects such as space charge forces and wake field interactions. Our Synergia simulations of the Booster with wake fields predict transverse tune shifts in good agreement with experiment [4].

The paper is organized as follows. In Section II we calculate the impedance and the wake functions for flat chambers with laminations. We discuss the approximations involved in the calculation at length. In Section III we perform a similar calculation for circular chambers with laminations and compare the results between the round and the flat chambers. We then employ Synergia for simulations of the beam dynamics in the Fermilab Booster and and compare the results with experimental data in Section IV.

II. PARALLEL-PLANE CHAMBER WITH LAMINATIONS

A. Wake functions

The wake functions describe the effect of the electromagnetic field created by a particle moving through an accelerator beam pipe upon the trailing particles. Consider a beam pipe enclosed between two parallel plates horizontally aligned. If the distance between the leading and trailing particle is $|z|$, the momentum of the trailing particle traversing a structure of length L will be modified by [5, 11]:

$$c\Delta p_z = -qQW^{||}(z) \tag{1}$$

$$c\Delta p_x = -qQ(W_x^{\perp}(z)X - W_x^{\perp}(z)x) \tag{2}$$

$$c\Delta p_y = -qQ(W_y^{\perp}(z)Y + W_x^{\perp}(z)y) \ . \tag{3}$$

Here Q (q) and (X, Y) ((x, y)) represent the charge and the transverse displacement of the leading (trailing) particle respectively. $||$ and $\perp$ denote the longitudinal and the transverse directions. The higher-order terms in the displacement are neglected. For this particular geometry, only two wake functions, $W_x^{\perp}(z)$ and $W_y^{\perp}(z)$, are needed for the transverse directions (Eq. 2 and Eq. 3). This is a consequence of the translational symmetry along the horizontal direction and of the Panofsky-Wenzel theorem which requires that $\frac{\partial \Delta p_x}{\partial x} = -\frac{\partial \Delta p_y}{\partial y}$. The terms proportional to the displacement of the leading particle, i.e., to X or Y, are called *dipole* wakes while the ones proportional to the displacement of the trailing particle, i.e., to x or y, are called *quadrupole* wakes [12]. Note that in a circular pipe the quadrupole wake fields vanish due to symmetry, while extra terms can be present in pipes with lower symmetries [11].

To calculate the electromagnetic field, often it is easier to solve the Maxwell equations in the frequency domain, and afterward calculate the impedances. Once the impedances are known the wakes can be obtained by a Fourier transform,

$$W^{||}(z) = \frac{1}{2\pi}\int d\omega Z^{||}(\omega)e^{-j\frac{\omega}{c}z} \tag{4}$$

$$W_{(x,y)}^{\perp}(z) = \frac{j}{2\pi}\int d\omega Z_{(x,y)}^{\perp}(\omega)e^{-j\frac{\omega}{c}z} \ . \tag{5}$$

In order to calculate the Fourier transforms, it is necessary to have accurate knowledge of the impedance $Z(\omega)$ over the whole frequency domain.

B. Impedance

The electromagnetic field inside a pipe with finite conductivity can be seen as a sum of two terms, one being the solution of the beam inside a pipe with the same geometry but with infinite conductivity and the rest. The first contribution to impedance is proportional to γ^{-2}, thus vanishing in the ultrarelativistic limit. The second contribution, referred to as the coupling impedance, is produced by currents in the pipe walls and is a consequence of their finite conductivity. Thus the ultrarelativistic coupling impedance is given by the solution of the Maxwell equations for an

ultrarelativistic beam in a pipe with finite conductivity. However the non-ultrarelativistic corrections to the coupling impedance can be important for low energy beams [13]. The calculation of impedance for non-ultrarelativistic beams will be presented elsewhere.

The purpose of this section is to write the coupling impedance as a function of the wall surface impedances for chamber with flat geometry. The surface impedances are given by the ratio of the different tangential components of the electric and the magnetic fields at the chamber's walls and are specific to the chamber. In the next two sections we will derive the surface impedances for the metallic and laminated chambers respectively.

Our derivation follows closely Ng's derivation [9]. Consider a relativistic beam propagating through the pipe with a vertical offset $y = a$. The distance between the parallel plates is $2b$. The charge density and the electrical current are given by

$$\rho(x,y,z,t) = \rho\delta(x)\delta(y-a)e^{j(\omega t - kz)} \tag{6}$$

$$\vec{J}(x,y,z,t) = \rho(x,y,z,t)\beta c\hat{z} \ , \tag{7}$$

with $k = \frac{\omega}{c}$. We look for synchronous solutions of the Maxwell equations:

$$\vec{E}(x,y,z,t) = \vec{E}(x,y)e^{j(\omega t - kz)} \tag{8}$$

$$\vec{H}(x,y,z,t) = \vec{H}(x,y)e^{j(\omega t - kz)} \ . \tag{9}$$

The spectral decomposition along the horizontal direction can be written as

$$(E_z(x,y), E_y(x,y), H_x(x,y)) = \int_{-\infty}^{\infty} (E_z(\eta,y), E_y(\eta,y), H_x(\eta,y)) \cos(\eta x) d\eta \tag{10}$$

$$(H_z(x,y), H_y(x,y), E_x(x,y)) = \int_{-\infty}^{\infty} (H_z(\eta,y), H_y(\eta,y), E_x(\eta,y)) \sin(\eta x) d\eta \ .$$

Inside the vacuum chamber, from the transverse components of the Maxwell equations, $\nabla \times E = -jkZ_0 H$ and $\nabla \times H = jkE$, one gets

$$\partial_y E_z = \eta Z_0 H_z \tag{11}$$

$$\partial_y Z_0 H_z = \eta E_z \ , \tag{12}$$

which results in

$$E_z(\eta,y) = A_\eta \cosh \eta y + \bar{A}_\eta \sinh \eta y \tag{13}$$

$$Z_0 H_z(\eta,y) = A_\eta \sinh \eta y + \bar{A}_\eta \cosh \eta y \ , \tag{14}$$

where $Z_0 \approx 377\Omega$ is the free space impedance. The transverse components of the fields can also be easily deduced. For a detailed derivation see K. Y. Ng [9]. The set of constants A_η and $\bar{A}_\eta$ are determined by imposing boundary conditions on the fields components at the pipe's walls. They are also uniquely determined if the surface impedances

$$\mathcal{R}_z(\eta) = \pm \left.\frac{E_z(\eta)}{H_x(\eta)}\right|_{y=\pm b} \tag{15}$$

$$\mathcal{R}_x(\eta) = \mp \left.\frac{E_x(\eta)}{H_z(\eta)}\right|_{y=\pm b} \tag{16}$$

at the pipe's walls are known, by substituting in the expressions for the fields and solving for the coefficients,

$$A_\eta = \frac{-\frac{\rho \mathcal{R}_z(\eta)}{2Z_0\epsilon_0} \ \mathrm{sech}^2 \eta b \ \cosh \eta a}{1 + j\frac{\mathcal{R}_z(\eta)}{Z_0}(\frac{k}{\eta} - \frac{\eta}{k}) \tanh \eta b + \frac{\mathcal{R}_z(\eta)\mathcal{R}_x(\eta)}{Z_0^2} \tanh^2 \eta b} \tag{17}$$

$$\bar{A}_\eta = \frac{-\frac{\rho \mathcal{R}_z(\eta)}{2Z_0\epsilon_0} \ \mathrm{csch}^2 \eta b \ \sinh \eta a}{1 + j\frac{\mathcal{R}_z(\eta)}{Z_0}(\frac{k}{\eta} - \frac{\eta}{k}) \coth \eta b + \frac{\mathcal{R}_z(\eta)\mathcal{R}_x(\eta)}{Z_0^2} \coth^2 \eta b} \ . \tag{18}$$

Now the problem of determining the constants A_η and $\bar{A}_\eta$ has changed into that of determining $\mathcal{R}_z$ and $\mathcal{R}_x$ from the boundary conditions.

The longitudinal and the transverse impedances can be written as a function of the longitudinal fields E_z and H_z. Thus, the longitudinal impedance is

$$\begin{aligned} Z^{||} &= -\frac{E_z(x=0,y=0)|_{a=0}}{\rho c} = -\frac{1}{2\pi\rho c}\int_{-\infty}^{\infty} d\eta A_\eta \\ &= \frac{1}{2\pi}\int_0^\infty d\eta \frac{\operatorname{sech}^2\eta b\ \mathcal{R}_z(\eta)}{1+j\frac{\mathcal{R}_z(\eta)}{Z_0}(\frac{k}{\eta}-\frac{\eta}{k})\tanh\eta b+\frac{\mathcal{R}_z(\eta)\mathcal{R}_x(\eta)}{Z_0^2}\tanh^2\eta b}\ , \end{aligned} \tag{19}$$

provided the surface impedances are even functions of η.

The vertical force acting upon a trailing charge q at $y=0$ created by a beam with displacement $y=a$, is

$$F_y(\eta, y=0) = q(E_y(\eta)+Z_0H_x(\eta)) = qj\frac{\eta}{k}Z_0H_z(\eta) = qj\frac{\eta}{k}\bar{A}_\eta\ . \tag{20}$$

The vertical impedance is

$$Z_y = -\frac{F_y(x=0,y=0)}{jq\rho ca} = \frac{1}{2\pi k}\int_0^\infty d\eta \frac{\eta^2\operatorname{csch}^2\eta b\ \mathcal{R}_z(\eta)}{1+j\frac{\mathcal{R}_z(\eta)}{Z_0}(\frac{k}{\eta}-\frac{\eta}{k})\coth\eta b+\frac{\mathcal{R}_z(\eta)\mathcal{R}_x(\eta)}{Z_0^2}\coth^2\eta b}\ , \tag{21}$$

where only the first order term in the beam displacement was retained, i.e. $\sinh\eta a \approx \eta a$.

The horizontal force acting upon a trailing charge q at $y=0$, by a centered beam is

$$F_x(\eta, y=0) = q(E_x(\eta)-Z_0H_y(\eta)) = qj\frac{\eta}{k}E_z(\eta) = qj\frac{\eta}{k}A_\eta|_{a=0}\ . \tag{22}$$

For small horizontal displacement of the trailing particle, $F_x(x=\Delta)\approx\Delta\frac{\partial F_x}{\partial x}(x=0)$. Note that $F_x(x)\propto\sin\eta x$ thus, $\frac{\partial F_x}{\partial x}\propto\eta\cos\eta x$. The horizontal impedance is

$$Z_x = -\frac{\Delta\frac{\partial F_x}{\partial x}(x=0,y=0)}{jq\rho c\Delta} = \frac{1}{2\pi k}\int_0^\infty d\eta \frac{\eta^2\operatorname{sech}^2\eta b\ \mathcal{R}_z(\eta)}{1+j\frac{\mathcal{R}_z(\eta)}{Z_0}(\frac{k}{\eta}-\frac{\eta}{k})\tanh\eta b+\frac{\mathcal{R}_z(\eta)\mathcal{R}_x(\eta)}{Z_0^2}\tanh^2\eta b}\ . \tag{23}$$

The integrands in Eq. 19, 21, and 23 are proportional to $\operatorname{sech}^2\eta b$ or $\operatorname{csch}^2\eta b$, thus going exponentially to zero for $\eta > \frac{1}{b}$. Therefore only the regime of small η, where $\eta < \frac{1}{b}$ is relevant for the impedance.

C. Resistive-wall impedance

The resistive-wall impedance for metallic flat pipes has been calculated by various authors [9, 14]. The main reason for presenting the derivation here is to take a critical look at the approximations involved. As we will see in Sec. II D, many of the assumptions valid for the metallic pipes do not hold when laminations are present.

The homogeneous Maxwell equations imply

$$(\frac{\partial^2}{\partial y^2}-k^2-\eta^2+\omega^2\epsilon\mu)\begin{pmatrix} E_z(\eta,y,k,\omega) \\ H_z(\eta,y,k,\omega)\end{pmatrix} = 0\ . \tag{24}$$

The solution for the fields inside the metallic pipe can be obtained by replacing the electric permittivity with

$$\epsilon \to \epsilon_0(\epsilon_r + \frac{\sigma}{j\omega\epsilon_0}) \tag{25}$$

where σ is the pipe conductivity and ϵ_r is the relative permittivity. One gets

$$\frac{\partial^2}{\partial y^2}\begin{pmatrix} E_z \\ H_z\end{pmatrix} = (\eta^2+\lambda_c^2+p^2)\begin{pmatrix} E_z \\ H_z\end{pmatrix} \tag{26}$$

where $\lambda_c^2 = j\omega\sigma\mu = jkZ_0\sigma\mu_r$, $p^2 = k^2(1-\epsilon_r\mu_r)$, and μ_r is the relative permeability. The solution for a infinitely thick pipe is [9]

$$\begin{aligned} &E_z = A_\eta\cosh\eta b\ e^{\lambda(b\mp y)} \\ &Z_0H_z = \pm A_\eta\sinh\eta b\ e^{\lambda(b\mp y)} \\ &E_x = \tfrac{A_\eta}{Z_0\sigma\mu_r - jk(1-\epsilon_r\mu_r)}(-\eta\cosh\eta b-\mu_r\lambda\sinh\eta b)\ e^{\lambda(b\mp y)} \\ &Z_0H_x = \tfrac{A_\eta}{Z_0\sigma\mu_r - jk(1-\epsilon_r\mu_r)}(\pm\lambda\cosh\eta b\pm\eta\sinh\eta b)\ e^{\lambda(b\mp y)} \mp \tfrac{j\lambda A_\eta}{k}\tfrac{Z_0\sigma}{Z_0\sigma\mu_r - jk(1-\epsilon_r\mu_r)}\cosh\eta b\ e^{\lambda(b\mp y)} \end{aligned} \tag{27}$$

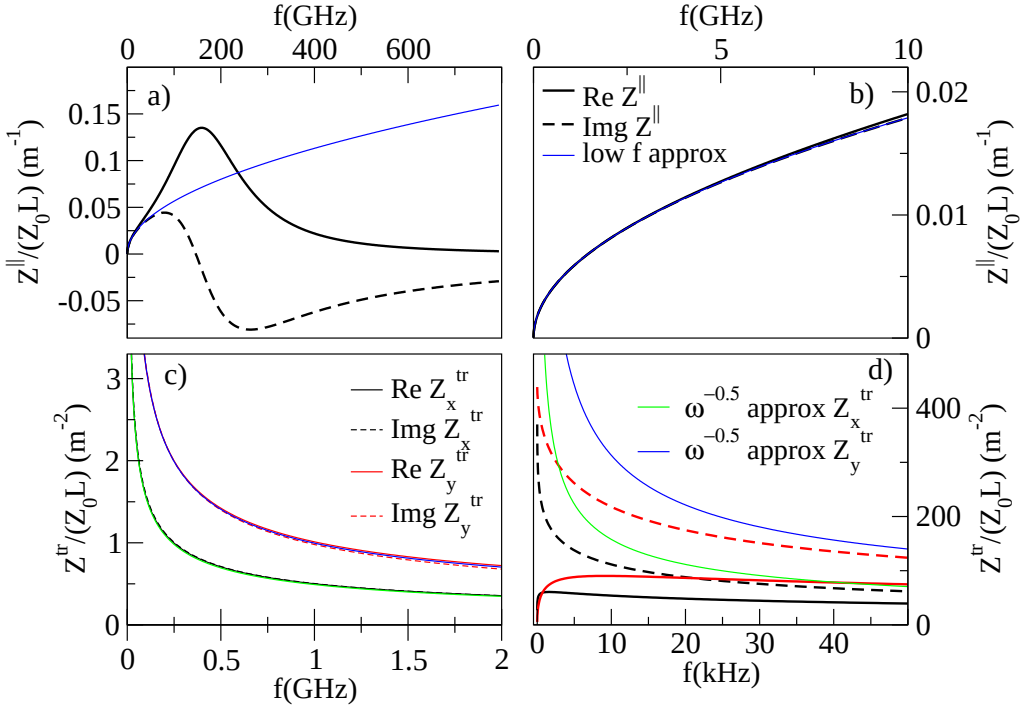

FIG. 1: Impedances of a parallel-plane iron pipe, $\sigma_{iron} = 0.5 \times 10^7 (\Omega m)^{-1}$ with $b = 0.02m$. a) and b) Real (black continuous) and imaginary (black dashed) longitudinal impedance, Eq.19. The low frequency approximation (blue) $\propto \sqrt{\omega}$, Eq.35, is valid up to $10GHz$. c) and d) Real and imaginary part of the horizontal (black continuous and black dashed) and the vertical (red continuous and red dashed) impedances, Eq. 23 and Eq. 21. Eq. 36 (green) and Eq. 37 (blue) are valid approximations in the interval range $1MHz - 2GHz$.

where $\lambda = \sqrt{\eta^2 + \lambda_c^2 + p^2}$. For surface impedance one gets

$$\frac{Z_0}{\mathcal{R}_z(\eta)} = \frac{1}{Z_0\sigma\mu_r - jk(1-\epsilon_r\mu_r)}(\lambda + \eta\tanh\eta b) - \frac{j\lambda}{k}\frac{Z_0\sigma}{Z_0\sigma\mu_r - jk(1-\epsilon_r\mu_r)} \tag{28}$$

$$\frac{\mathcal{R}_x(\eta)}{Z_0} = \frac{1}{Z_0\sigma\mu_r - jk(1-\epsilon_r\mu_r)}(\eta\coth\eta b + \mu_r\lambda) \tag{29}$$

The coupling impedances follow immediately by putting Eq. 28 and Eq. 29 into equations 19, 21 and 23.

Due to the large value of the conductivity in metallic pipes, $Z_0\sigma \approx 10^8 - 10^9 m^{-1}$, several simplifying approximations are commonly used. $Z_0\sigma\mu_r \gg jk(1-\epsilon_r\mu_r)$ up to very high frequencies, $\omega <\approx 10^6 GHz$. Thus the term $jk(1-\epsilon_r\mu_r)$ can be neglected. As pointed at the end of Sec. II B, only values of $\eta < \frac{1}{b} \approx 10^2 m^{-1}$ are relevant, provided the pipe radius is of the order of centimeters. Thus

$$\lambda \approx \lambda_c = \frac{1+j}{\delta} \ , \tag{30}$$

where $\delta = \sqrt{\frac{2}{\omega\sigma\mu}}$ is the skin penetration depth. The first two terms in Eq. 28 are $\mathcal{O}(\frac{1}{Z_0\sigma})$ relative to the third one, and thus can be neglected. In addition, the first term in Eq. 29 is $\mathcal{O}(\frac{1}{\sqrt{Z_0\sigma}})$ relative to the second one. Therefore

$$\mathcal{R}_z(\eta), \mathcal{R}_x(\eta) \approx \frac{\lambda_c}{\sigma} = \frac{1+j}{\delta\sigma} \ . \tag{31}$$

The surface impedances are small, $\mathcal{O}(\frac{1}{\sqrt{\sigma}})$. For this reason the higher-order terms in the surface impedances in the denominator of Eq. 19, Eq. 21 and Eq. 23 are not very important in the relevant frequency region for the beam dynamics. The term proportional to $\mathcal{R}_z(\eta)\mathcal{R}_x(\eta)$ is negligible. The term proportional to $\frac{\mathcal{R}_z}{Z_0}\frac{k}{\eta}$ determines the high frequency behavior ($k >\approx \frac{Z_0}{b\mathcal{R}_z}$) and the one proportional to $\frac{\mathcal{R}_z}{Z_0}\frac{\eta}{k}$ the low frequency behavior ($k <\approx \frac{\mathcal{R}_z}{bZ_0}$). These

terms proportional to $\mathcal{R}_z$ are also small and are often neglected. Thus

$$Z^{||} = \frac{1}{2\pi}\int_0^\infty d\eta \,\mathrm{sech}^2\,\eta b\;\mathcal{R}_z(\eta)\;, \tag{32}$$

$$Z_x = \frac{1}{2\pi k}\int_0^\infty d\eta\eta^2\,\mathrm{sech}^2\,\eta b\;\mathcal{R}_z(\eta)\;, \tag{33}$$

$$Z_y = \frac{1}{2\pi k}\int_0^\infty d\eta\eta^2\,\mathrm{csch}^2\,\eta b\;\mathcal{R}_z(\eta)\;. \tag{34}$$

Since $\mathcal{R}_z$ is weakly dependent on η, the common approximations used in the literature for studying impedance effects in metallic pipes are

$$Z^{||} = \frac{\mathcal{R}_z}{2\pi b}, \tag{35}$$

$$Z_x = \frac{\mathcal{R}_z}{2\pi k}\frac{\pi^2}{12b^3}\;, \tag{36}$$

$$Z_y = \frac{\mathcal{R}_z}{2\pi k}\frac{\pi^2}{6b^3}\;, \tag{37}$$

with $\mathcal{R}_z(\eta) \approx \mathcal{R}_z(\eta = 0)$. In this approximation $Z^{||} \propto \sqrt{\omega}$, while the $Z_{x,y} \propto \frac{1}{\sqrt{\omega}}$ and diverges when $\omega \to 0$. If the low frequency behavior is important one can employ

$$Z_x = \frac{\mathcal{R}_z}{2\pi k}\int_0^\infty d\eta \frac{\eta^2\,\mathrm{sech}^2\,\eta b}{1 - \frac{j\mathcal{R}_z\eta}{Z_0 k}\tanh\eta b}\;, \tag{38}$$

$$Z_y = \frac{\mathcal{R}_z}{2\pi k}\int_0^\infty d\eta \frac{\eta^2\,\mathrm{csch}^2\,\eta b}{1 - \frac{j\mathcal{R}_z\eta}{Z_0 k}\coth\eta b}\;, \tag{39}$$

which removes the low frequency divergence and makes the real part of the transverse impedance to go to zero and the imaginary part to approach a constant when $\omega \to 0$.

The impedance of an iron pipe with $b = 2cm$ and the commonly employed approximations for a metallic pipe discussed previously are illustrated in Fig. 1. Subfigures 1a and 1b show the longitudinal impedance and the approximations employed by Eq. 35 which holds up to $10GHz$. The horizontal and the vertical impedances and the approximations given by Eq. 36 and Eq. 37 are shown in subfigs. 1c and 1d. The approximations are valid in the frequency interval $1MHz - 2GHz$ which corresponds to $8mm - 16m$ in the reciprocal space. One concludes that the commonly used approximations for resistive-wall impedance are valid to investigate the wake effects in metallic pipes at distances of the order of centimeters and meters.

However, when the surface impedance is large the resistive-wall metallic pipe approximations, i.e. Eq. 35, Eq. 36 and Eq. 37, are not valid anymore. Since in general the laminations increase the surface impedance by more than two orders of magnitude, this is an important aspect which should be accounted for when calculating the impedance in laminated structures. In Fig. 2 the impedance is plotted for a pipe with a much smaller conductivity than iron, $\sigma = \sigma_{iron} \times 10^{-4}$. According to Eq. 31 this corresponds to a 100 times larger surface impedance. The approximation $Z^{||} \propto \sqrt{\omega}$ (Eq. 35) commonly used for the longitudinal impedance, does not hold. A better low frequency approximation,

$$Z^{||} = \frac{1}{2\pi}\int_0^\infty d\eta \frac{\mathrm{sech}^2\,\eta b\;\mathcal{R}_z(\eta)}{1 - j\frac{\mathcal{R}_z(\eta)}{Z_0}\frac{\eta}{k}\tanh\eta b}\;, \tag{40}$$

can be used, but only up to $\simeq 500MHz$. Eq. 36 and Eq. 37 do not work for the transverse impedance either. One can see in Fig. 2c that the real and the imaginary part of the transverse impedances are different. Eq. 38 and Eq. 39 hold only below $200MHz$. The only term which can be safely neglected in the denominator of Eqs. 19, 23 and 21 is the one proportional to $\mathcal{R}_z\mathcal{R}_x$.

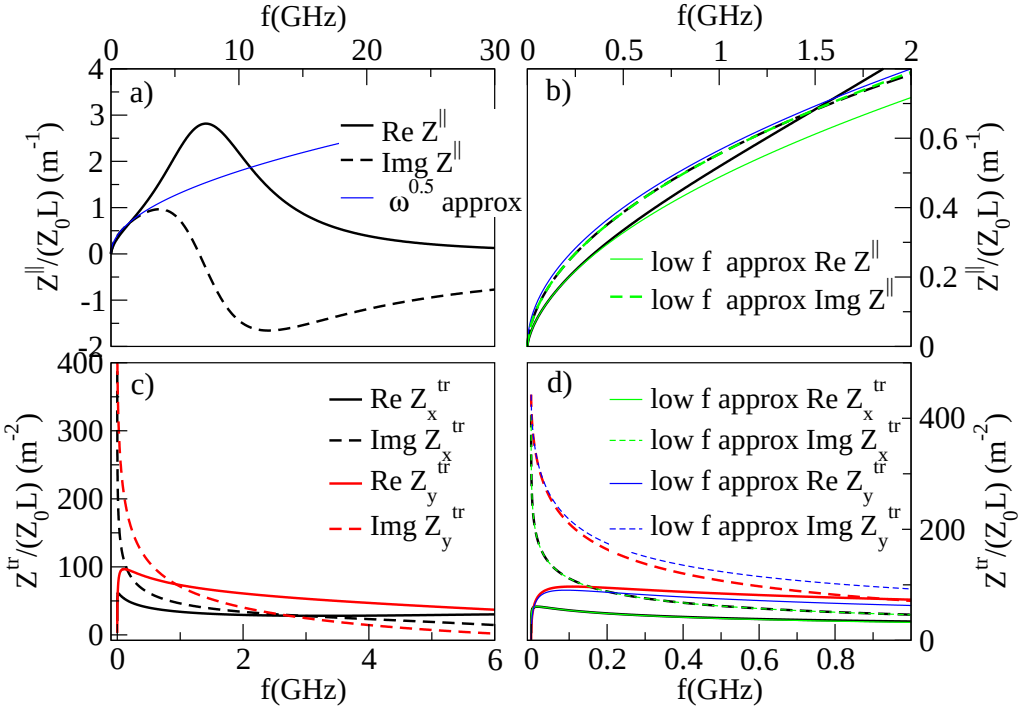

FIG. 2: Impedances of a parallel-plane pipe with $\sigma = \sigma_{iron} \times 10^{-4}$ with $b = 0.02m$. a) and b) Real (black continuous) and imaginary (black dashed) longitudinal impedance, Eq.19. The low frequency approximation (blue) $\propto \sqrt{\omega}$, Eq.35 (blue) is not valid, while Eq.40 (green) approximation hold up to $500MHz$. c) and d) Real and imaginary part of the horizontal (black continuous and black dashed) and the vertical (red continuous and red dashed) impedances, Eq. 23 and Eq. 21. Eq. 36 and Eq. 37 are not valid approximations, while Eq. 38 (green) and Eq. 39 (blue) are good only up to $200MHz$.

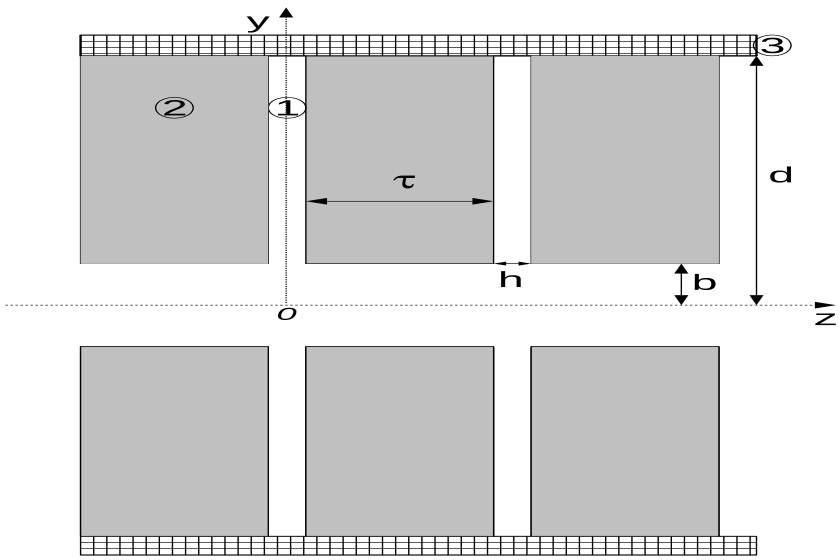

FIG. 3: Parallel-plane beam chamber with laminations. Subscript "1" denotes the crack and subscript "2" the lamination. The laminations are shorted by an ideal conductor "3". The beam flows in the z-direction; the x-direction is perpendicular to the plane of the page.

D. Laminated structures

A chamber with parallel faces and a laminated structure is sketched in Fig. 3. The subscript "1" denotes the dielectric crack of width h, and "2" denotes the metallic lamination of width τ. The conductivity is large in the laminations σ_2 ($\approx 10^7(\Omega m)^{-1}$); it is assumed that the dimension $\tau + h$ is small ($\approx 10^{-3} - 10^{-4} m$) compared to the propagation wavelength.

With the above assumptions, the formalism presented in Sec. II B is valid and the coupling impedance can be written as a function of the chamber surface impedance. To show this, we start with the following definition of the longitudinal impedance [15]

$$Z^{||}(\omega) = -\frac{1}{\rho c} \int dz E_z(z,\omega)\Big|_{x,y=0} e^{-j\frac{\omega}{c}z} \ . \tag{41}$$

Since the longitudinal dimension of laminations and cracks is small compared to the propagation wavelength, i.e. $\frac{\omega}{c}(\tau + h) \ll 1$, the following approximation is valid

$$Z^{||}(\omega) \approx -\frac{1}{\rho c} \sum_{n=-\infty}^{\infty} (\tau + h)\bar{E}_z(z_n,\omega)|_{x,y=0} \ e^{-j\frac{\omega}{c}z_n} \tag{42}$$

where $z_n = n(\tau + h)$ is chosen to be in the middle of the crack "n", and

$$\bar{E}_z(z_n,\omega) = \frac{1}{\tau + h}\left(\int_{z_n-h/2}^{z_n+h/2} E_{z1}(z,\omega)dz + \int_{z_n-h/2-\tau}^{z_n-h/2} E_{z2}(z,\omega)dz\right) = \frac{\bar{E}_{z1}(z_n,\omega)h + \bar{E}_{z2}(z_n,\omega)\tau}{\tau + h} \ , \tag{43}$$

represents the average field integrated over one lamination width and one crack width. Thus the surface impedances should be defined as

$$\bar{\mathcal{R}}_z(\omega,\eta) = \frac{\sum_n \bar{E}_z(z_n,\omega,\eta)e^{-j\frac{\omega}{c}z_n}}{\sum_n \bar{H}_x(z_n,\omega,\eta)e^{-j\frac{\omega}{c}z_n}}\Bigg|_{y=b} = \frac{\bar{E}_z(z=0,\omega,\eta)}{\bar{H}_x(z=0,\omega,\eta)}\Bigg|_{y=b} \ , \tag{44}$$

provided $\frac{\bar{E}_z(z_n,\omega,\eta)}{\bar{H}_x(z_n,\omega,\eta)}\Big|_{y=b}$ does not depend on z_n.

Before calculating the surface impedance for the laminated structures some simplifications are in order. Using Eq. 43 one can write

$$\bar{\mathcal{R}}_z(\omega,\eta) = \frac{\bar{E}_{z1}h + \bar{E}_{z2}\tau}{\bar{H}_{x1}h + \bar{H}_{x2}\tau}\Bigg|_{y=b} \ . \tag{45}$$

As will be discussed at the end of Sec. II D 1, at the pipe wall

$$\bar{H}_{x1}|_{y=b} \approx \bar{H}_{x2}|_{y=b} \ . \tag{46}$$

Therefore

$$\bar{\mathcal{R}}_z = \frac{\mathcal{R}_{1z}h + \mathcal{R}_{2z}\tau}{h + \tau} \tag{47}$$

where $\mathcal{R}_{1z} = \frac{\bar{E}_{z1}}{\bar{H}_{x1}}\Big|_{y=b}$ and $\mathcal{R}_{2z} = \frac{\bar{E}_{z2}}{\bar{H}_{x2}}\Big|_{y=b}$ represent the longitudinal surface impedance in the crack and in the lamination respectively.

Similarly, the horizontal surface impedance is

$$\bar{\mathcal{R}}_x(\omega) = -\frac{\bar{E}_{x1}h + \bar{E}_{x2}\tau}{\bar{H}_{z1}h + \bar{H}_{z2}\tau}\Bigg|_{y=b} \ . \tag{48}$$

Since $\bar{H}_{z1}, \bar{E}_{x1} \approx 0$, as will be discussed at the end of Sec. II D 1,

$$\bar{\mathcal{R}}_x(\omega) \approx -\frac{\bar{E}_{x2}}{\bar{H}_{z2}}\Bigg|_{y=b} \approx \mathcal{R}_{2x} \ . \tag{49}$$

1. Surface impedance

In order to calculate the surface impedance, focus on the regions 1 and 2 shown in Fig. 3, i.e. $y > b$, and choose the middle of the crack as the origin ($z = 0$), also shown in the figure. Assume that the field-dependence along the z-direction can be described by

$$\frac{\partial^2 E_z}{\partial z^2} = g_{1,2}^2 E_z \tag{50}$$

$$\frac{\partial^2 H_z}{\partial z^2} = g_{1,2}^2 H_z \tag{51}$$

where the subscripts 1 and 2 correspond to the crack and lamination respectively. The field equation is

$$(\frac{\partial^2}{\partial y^2} - \eta^2 + g_{1,2}^2 + \omega^2\mu\epsilon)\begin{pmatrix} E_z \\ H_z \end{pmatrix} = 0 \ . \tag{52}$$

Region 1. Denoting $q^2 = \omega^2\mu_1\epsilon_1 + g_1^2 - \eta^2$, the solution of Eq. 52 inside the crack is

$$E_z = A_1 \cosh(g_1 z)(\sin qy + \alpha \cos qy)\cos \eta x \tag{53}$$

$$Z_0 H_z = B_1 \sinh(g_1 z)(\alpha \sin qy - \cos qy)\sin \eta x \ . \tag{54}$$

The transverse fields can be determined from the longitudinal fields[16], thus

$$(\omega^2\mu_1\epsilon_1 + g_1^2)E_x = (-A_1\eta g_1 - B_1 j\omega q\frac{\mu_{1r}}{c})\sinh(g_1 z)(\sin qy + \alpha\cos qy)\sin\eta x \tag{55}$$

$$(\omega^2\mu_1\epsilon_1 + g_1^2)Z_0 H_x = (-A_1 j\omega q\frac{\epsilon_{1r}}{c} + B_1\eta g_1)\cosh(g_1 z)(\alpha\sin qy - \cos qy)\cos\eta x \tag{56}$$

$$(\omega^2\mu_1\epsilon_1 + g_1^2)E_y = (-A_1 q g_1 + B_1 j\omega\eta\frac{\mu_{1r}}{c})\sinh(g_1 z)(\alpha\sin qy - \cos qy)\cos\eta x \tag{57}$$

$$(\omega^2\mu_1\epsilon_1 + g_1^2)Z_0 H_y = (A_1 j\omega\eta\frac{\epsilon_{1r}}{c} + B_1 q g_1)\cosh(g_1 z)(\sin qy + \alpha\cos qy)\sin\eta x \tag{58}$$

For the sake of simplicity, we assume that the crack terminates at $y = d$ in an ideal conductor. The condition $E_z|_{y=d} = 0$ implies

$$\alpha = -\tan(qd) \tag{59}$$

The same constant α appears in the expression of all field components as written in Eq. 54-58. This is a consequence of the condition $H_y|_{y=d} = 0$. $E_y \propto \sinh(g_1 z)$, since the current J_y in the laminations along the crack goes in the opposite direction on the two sides of the crack. The dependence of the other field components on the sign of z follows from the Maxwell equations.

Region 2. Analogously, inside the lamination and close to the crack-lamination boundary

$$E_z = A_2 e^{-g_2|z|}(\sin qy + \alpha\cos qy)\cos\eta x \tag{60}$$

$$H_z = B_2 e^{-g_2|z|} sgn(z)(\alpha\sin qy - \cos qy)\sin\eta x \tag{61}$$

$$(\omega^2\mu_2\epsilon_2 + g_2^2)E_x = (A_2\eta g_2 - B_2 j\omega q\frac{\mu_{2r}}{c})e^{-g_2|z|}sgn(z)(\sin qy + \alpha\cos qy)\sin\eta x \tag{62}$$

$$(\omega^2\mu_2\epsilon_2 + g_2^2)Z_0 H_x = (-A_2 j\omega q\frac{\epsilon_{2r}}{c} - B_2\eta g_2)e^{-g_2|z|}(\alpha\sin qy - \cos qy)\cos\eta x \tag{63}$$

$$(\omega^2\mu_2\epsilon_2 + g_2^2)E_y = (A_2 q g_2 + B_2 j\omega\eta\frac{\mu_{2r}}{c})e^{-g_2|z|}sgn(z)(\alpha\sin qy - \cos qy)\cos\eta x \tag{64}$$

$$(\omega^2\mu_2\epsilon_2 + g_2^2)Z_0 H_y = (A_2 j\omega\eta\frac{\epsilon_{2r}}{c} - B_2 q g_2)e^{-g_2|z|}(\sin qy + \alpha\cos qy)\sin\eta x \ . \tag{65}$$

Only the exponentially decaying terms proportional to $e^{-g_2|z|}$ describe the fields in the laminations since it is assumed that the skin penetration depth is much less than the lamination thickness $\delta_2 \ll \tau$. The continuity of the fields at $z = \pm h/2$ implies

$$q^2 = \omega^2\mu_2\epsilon_2 + g_2^2 - \eta^2 = \omega^2\mu_1\epsilon_1 + g_1^2 - \eta^2. \tag{66}$$

Finding g_1 turns out to be enough for the calculation of the surface impedance. Since an exact solution requires substantial numerical effort, requiring field matching at the crack-lamination and pipe-wall boundaries, we take

advantage of the high conductivity σ_2 in the laminations to provide an approximate solution. Note that if the laminations were ideal conductors then $E_y, E_x, H_z|_{z=\pm h/2} = 0$. This implies either

$$g_1(\sigma_2 \to \infty) \to 0 \ , \tag{67}$$

or

$$A_1(\sigma_2 \to \infty) \to 0 \tag{68}$$

and

$$B_1(\sigma_2 \to \infty) \to 0 \ . \tag{69}$$

The latter case yields a solution with a small electric field E_z for large σ_2, thus giving a small contribution to the surface impedance. So, that case will be neglected to look for solutions which fulfill Eq. 67.

By imposing the continuity of E_x, E_y, H_x and H_y at $z = h/2$ one gets

$$\frac{A_1}{A_2} = -\frac{(\eta g_2 - \frac{B_2}{A_2} j\omega q \frac{\mu_{2r}}{c})e^{-g_2 h/2}}{(\eta g_1 + \frac{B_1}{A_1} j\omega q \frac{\mu_{1r}}{c}) \sinh(g_1 h/2)} \tag{70}$$

$$= -\frac{(q g_2 + \frac{B_2}{A_2} j\omega \eta \frac{\mu_{2r}}{c})e^{-g_2 h/2}}{(q g_1 - \frac{B_1}{A_1} j\omega \eta \frac{\mu_{1r}}{c}) \sinh(g_1 h/2)} \tag{71}$$

$$= \frac{(j\omega q \frac{\epsilon_{2r}}{c} + \frac{B_2}{A_2} \eta g_2)e^{-g_2 h/2}}{(j\omega q \frac{\epsilon_{1r}}{c} - \frac{B_1}{A_1} \eta g_1) \cosh(g_1 h/2)} \tag{72}$$

$$= \frac{(j\omega \eta \frac{\epsilon_{2r}}{c} - \frac{B_2}{A_2} q g_2)e^{-g_2 h/2}}{(j\omega \eta \frac{\epsilon_{1r}}{c} + \frac{B_1}{A_1} q g_1) \cosh(g_1 h/2)} \ . \tag{73}$$

Eq. 70 and Eq. 73 yield

$$\frac{B_2}{A_2} = -\frac{B_1}{A_1} \frac{\mu_1 g_2}{\mu_2 g_1} \tag{74}$$

$$\frac{B_2}{A_2} = -\frac{B_1}{A_1} \frac{\epsilon_2 g_1}{\epsilon_1 g_2} \ . \tag{75}$$

If $B_1 \neq 0$ and $B_2 \neq 0$, Eq. 74 and Eq. 75 together with Eq. 66 imply

$$g_1^2 = -\omega^2 \epsilon_1 \mu_1 = -\frac{\omega^2}{c^2} \epsilon_{1r} \ , \tag{76}$$

$$g_2^2 = -\omega^2 \epsilon_2 \mu_2 \ . \tag{77}$$

One can immediately see that this solution is not in agreement with the requirement of Eq. 67. If $B_1 = 0$ and $B_2 = 0$ then it follows from Eq. 71 and Eq. 72 that

$$\frac{g_2 e^{-g_2 h/2}}{g_1 \sinh(g_1 h/2)} = -\frac{\epsilon_2 e^{-g_2 h/2}}{\epsilon_1 \cosh(g_1 h/2)} \tag{78}$$

or

$$g_1 \tanh(g_1 h/2) = -\frac{\epsilon_1}{\epsilon_2} g_2 \ . \tag{79}$$

g_2 is large and represents the field decaying parameter inside the laminations. In the relevant frequency domain g_2 has the following form[9, 16]

$$g_2 \approx \frac{1+j}{\delta_2} = \frac{(1+j)\sqrt{\omega \sigma_2 \mu_2}}{\sqrt{2}} \ . \tag{80}$$

Since $\epsilon_2 \approx \frac{\sigma_2}{j\omega}$ and $g_1 h \ll 1$

$$g_1^2 = -\frac{2 j g_2 \epsilon_1 \omega}{h \sigma_2} = (1-j)\omega^2 \epsilon_1 \mu_1 \frac{\mu_2}{\mu_1} \frac{\delta}{h} \ . \tag{81}$$

This solution for g_1 obeys Eq. 67 and is the same as the one given by Ng in [9] where only the $\eta = 0$ case was considered. However note that while g_1 here and in Ref [9] are the same, the surface impedance is significantly different.

The longitudinal surface impedance of the crack follows from Eq. 53 and Eq. 56

$$\frac{\mathcal{R}_{1z}(\eta,\omega)}{Z_0} = j\frac{q^2+\eta^2}{q\frac{\omega}{c}\epsilon_{1r}}\tan q(d-b) \tag{82}$$

where

$$q^2 = \omega^2\epsilon_1\mu_1\left[(1+(1-j)\frac{\mu_2}{\mu_1}\frac{\delta}{h}\right] - \eta^2 \ . \tag{83}$$

The difference between this solution and that in Ref. [9] is the presence of the η^2 term in Eq. 83.

The lamination longitudinal and horizontal surface impedances are

$$\mathcal{R}_{2z} \approx \frac{1+j}{\delta_2\sigma_2} \ , \tag{84}$$

and

$$\mathcal{R}_{2x} \approx \frac{1+j}{\delta_2\sigma_2} \ , \tag{85}$$

which are equal to the usual metal-vacuum boundary surface impedance. The surface impedances $\mathcal{R}_z$ and $\mathcal{R}_x$ can be simply obtained now by employing Eq. 47 and Eq. 49. Note that, unlike the resistive-wall case, the surface impedance is η dependent. This turns out to have a significant effect on the impedance.

We now justify the approximations made in Eq. 46 and Eq. 49:

- *Justification of Eq. 46.* Since $\tau \gg \delta_2$, away from the crack and at the lamination-chamber boundary (i.e. $y = +0+b$), the electromagnetic field decays along the vertical direction as

$$\frac{\partial^2 H_{x2}}{\partial y^2} \approx g_2^2 H_{x2} \tag{86}$$

  which implies

$$(\frac{\partial^2}{\partial z^2} - \eta^2 + g_2^2 + \omega^2\epsilon_2\mu_2)H_{x2} = 0 \ . \tag{87}$$

  Thus $H_{x2} \propto \cos(qz)$ away from the crack-lamination boundary. Since $q \sim \eta \sim \frac{1}{b}$ implies $q\tau \ll 1$, to a good approximation H_{x2} is constant along the z-direction in this region. The next region we focus on is the lamination close to both chamber and crack boundary. Inside the chamber (i.e. $y = -0+b$), the electric field component becomes very small $E_y(z \to \pm h/2) \to \mathcal{O}(\sigma_2^{-\frac{1}{2}})$ since it goes from being perpendicular to to parallel to a metallic surface. This implies that the variation of H_{x2} with z decreases in this region, because $\partial_z H_{x2} = j\omega\epsilon_0 E_y + \partial_x H_{z2}$. So far it has been argued that H_{x2} is nearly constant at the lamination-chamber boundary. In the crack, since $g_1 h \ll 1$, H_{x1} is also approximately constant along z-direction. The continuity of H_x at $z = \pm h/2$ and $y = b$ implies $\bar{H}_{x1}|_{y=b} \approx \bar{H}_{x2}|_{y=b}$.

- *Justification of Eq. 49.* Since $H_{z1}, E_{x1} \propto \sinh(g_1 z)$, their averaged value over the crack width is zero.

2. Coupling Impedance

Using the surface impedance calculated in the previous section, the impedance of a laminated chamber is obtained by employing Eq. 19, Eq. 21 and Eq. 23. Here we illustrate an example specific to the Fermilab Booster F-magnets, which have iron laminations. The chamber parameters are given in the caption of Fig. 4.

The longitudinal impedance is shown in Figs. 4a and 4b. It has a very different behavior than a resistive-wall impedance. At low frequencies, up to 30 $MHz \sim 40$ MHz, it increases with increasing frequency, then in the interval 50 $MHz \sim 200$ MHz it displays two broad and weakly developed peaks. A $\omega^{-\frac{1}{4}}$ behavior[8, 9] follows up to $6GHz$.

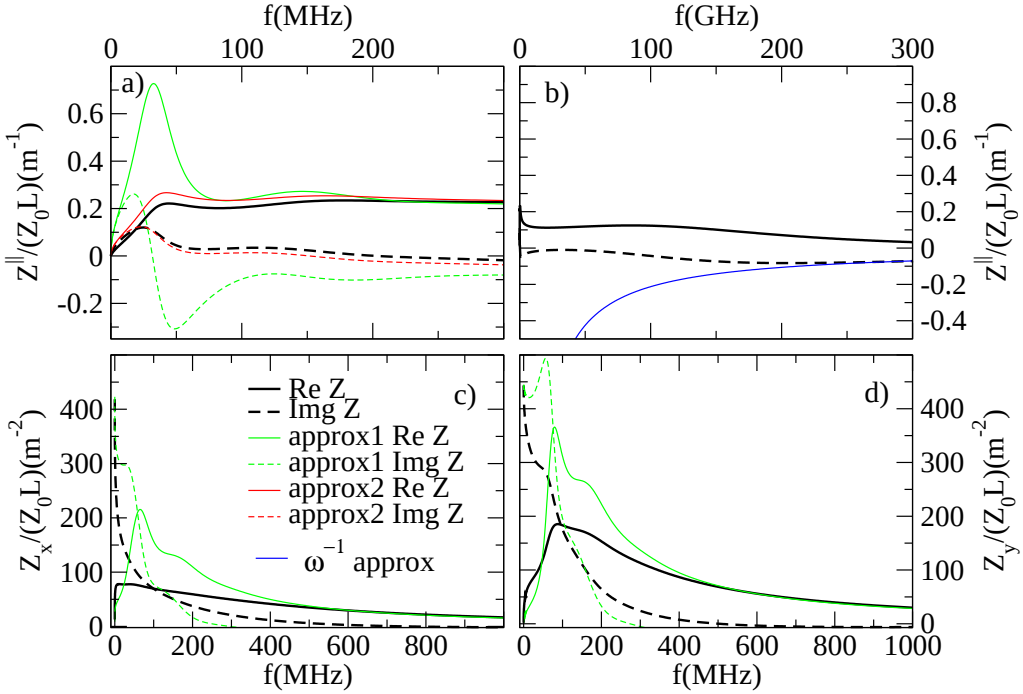

FIG. 4: Coupling impedances of a parallel-plane laminated chamber. We take $b = 2.1cm$, $d = 15.24cm$, $h = 9.52 \times 10^{-4}cm$, $\tau = 6.35 \times 10^{-2}cm$, $\epsilon_{1r} = 4.75$, $\mu_{2r} = 100$, and $\sigma_2 = 0.5 \times 10^7(\Omega m)^{-1}$ (iron), parameters specific to the Fermilab Booster F-magnets. The real (imaginary) part is plotted with full (dashed) lines. The black lines show the full impedance calculation done by employing Eq. 19, Eq. 21 and Eq. 23. Different approximations are also shown. The green lines are calculated by neglecting the η-dependence of the surface impedance, i.e. by making the approximation $\mathcal{R}_z(\eta) \approx \mathcal{R}_z(\eta = 0)$ and employing Eq. 35, Eq. 38 and Eq. 39. a) Low frequency and b) high frequency longitudinal impedance. The red lines are calculated by considering the full η-dependence of the surface impedance and by neglecting the terms proportional to the surface impedance in the denominator of Eq. 19, i.e. by employing Eq. 32. c) Horizontal transverse impedance. d) Vertical transverse impedance. The impedance is about two orders of magnitude larger than one corresponding to a resistive wall pipe made from the same material as the laminations. Note that neglecting the η dependence in the surface impedance yields values that are too large for the coupling impedance.

A third broad peak can be observed in the interval $20GHz \sim 80GHz$ and then the expected ω^{-1} behavior sets in at frequencies higher than $200GHz$.

The two commonly used approximations for the resistive-wall impedance, namely neglecting the $\mathcal{R}_z$-dependence on the horizontal wave-vector η and neglecting the terms proportional to $\mathcal{R}_z$ in the denominator of Eq. 19 do not hold for laminated structures. The former was assumed by Ng[9] while the latter was implicitly assumed in Refs. [7, 8] where the simple relation given by Eq. 35 between the surface impedance and the longitudinal coupling impedance was considered. The approximation Eq. 35 with $\mathcal{R}_z(\eta) \approx \mathcal{R}_z(\eta = 0)$, valid for metallic pipes, is also plotted in Fig. 4a. As one can see, Eq. 35 yields a much larger impedance for frequencies below $500MHz$.

In order to understand the importance of the η-dependence of $\mathcal{R}_z$ we will neglect for now the terms proportional to $\mathcal{R}_z$ in the denominator of Eq. 19 and will compare Eq. 32 versus Eq. 35 with $\mathcal{R}_z(\eta) \approx \mathcal{R}_z(\eta = 0)$. In the latter case, one gets at low frequencies $q^2 \approx (1-j)\omega^2\epsilon_1\mu_2\frac{\delta}{h}$, $R_z \approx \frac{\mathcal{R}_{1z}h}{h+\tau} = j\frac{q^2}{\epsilon_1}(d-b)$ and

$$Z^{||} = \frac{1}{2\pi b}\frac{1+j}{\sigma_2\delta_2}\frac{2(d-b)}{h+\tau} \ . \tag{88}$$

When the η-dependence is considered, at low frequency $q^2 = -\eta^2$, the impedance is

$$Z^{||} = \frac{2}{2\pi(h+\tau)}\frac{1+j}{\sigma_2\delta_2}\int_0^\infty d\eta\, \mathrm{sech}^2\,\eta b\frac{\tanh\eta(d-b)}{\eta} \ . \tag{89}$$

In the case $\frac{d-b}{b} \ll 1$, the integral in Eq. 89 is $\frac{d-b}{b}$ and the impedance has the same form as in Eq. 88. However, when

$\frac{d-b}{b} \gg 1$, as in our example, the integral is

$$\int_0^\infty d\eta \,\mathrm{sech}^2\, \eta b \frac{\tanh \eta(d-b)}{\eta} \approx \int_0^b d\eta \frac{\tanh \eta(d-b)}{\eta} \tag{90}$$
$$\approx \int_0^{\frac{1}{d-b}} d\eta \frac{\eta(d-b)}{\eta} + \int_{\frac{1}{d-b}}^b d\eta \frac{1}{\eta} = 1 + \ln \frac{d-b}{b} \approx \ln \frac{d-b}{b} \ ,$$

and

$$Z^{||} = \frac{1}{2\pi b} \frac{1+j}{\sigma_2 \delta_2} \frac{2}{h+\tau} b \ln \frac{(d-b)}{b} \ . \tag{91}$$

Thus, at low frequencies and to first order in $\mathcal{R}_z$, the impedance increases logarithmically with $d-b$ when d is large, similarly to the case of circular geometry (see Section III and [9]) and not linearly as one would wrongly infer if the η-dependence were neglected.

Besides considering the η-dependence of $\mathcal{R}_z$, taking into account terms proportional to $\mathcal{R}_z$ in the denominator of Eq. 19 is also important. The reason, as discussed in Sec. II C, is that $\mathcal{R}_z$ is large when the laminations are present, being enhanced roughly by a factor of $\frac{2b}{h+\tau} \ln \frac{d-b}{b}$ (which in our example is ≈ 115) compared to the resistive-wall case. The approximation given by Eq. 32, shown in red in Fig. 4a, although taking into account the η-dependence of $\mathcal{R}_z$, neglects the $\mathcal{R}_z$ terms in the denominator of Eq. 19. The low frequency behavior is given by Eq. 89 and has a $\sqrt{\omega}$ behavior. However this approximation differs from the full calculation (black) which yields a smaller impedance.

The horizontal and the vertical impedances are shown in Figs. 4c and 4d, respectively. Compared to the resistive-wall impedances for an iron chamber with the same dimensions (Fig. 1) they are about two orders of magnitude larger. For frequencies larger than $15MHz$, the vertical impedance is about two times larger than the horizontal one, a behavior characteristic of parallel-plane geometry [14]. The large frequency asymptotic behavior is $\omega^{-5/4}$. Note that the η-dependence of $\mathcal{R}_z$ is also important for the transverse impedances. Neglecting it would yield a much larger value for the impedance, as shown by the green lines where Eqs. 38 and 39, respectively, are employed.

3. *Wake functions*

The wake functions calculated from the impedances shown in Fig. 4 and calculated via Eqs. 4 and 5 are displayed in Fig. 5. For comparison different approximations and the resistive-wall impedance of an iron chamber with the same dimensions are also illustrated.

The longitudinal wake, shown in black in Fig. 5a, is repulsive at distances shorter than 0.2 m, while it becomes attractive at somewhat larger distances, with a maximum around $|z| \approx 0.4$ m. It decreases rapidly to zero at large distances. In the attractive region, at distances on the order of meters (which is usually of the same order as the bunch length in typical machines) it is much larger than the resistive wall impedance (blue). Note that the approximation based on Eq. 35, which neglects the η-dependence of $\mathcal{R}_z$ (green), yields a larger wake, repulsive for $|z| < 2$ m. Neglecting the $\mathcal{R}_z$ terms in the denominators of Eq. 19 (red) yields a smaller impedance at distances of the order of one meter.

The horizontal and vertical wakes are shown in Figs. 5b and 5c, respectively. The vertical wake is about two times larger than the horizontal one for distances of order of meters. In the same region the wakes are much larger than the corresponding resistive wall wakes (blue), but decay faster at large $|z|$. The neglect of the η-dependence of $\mathcal{R}_z$ (green) has a noticeable effect, yielding larger transverse wakes. The wiggling behavior of the vertical wake, seen in the inset of Fig. 5c is caused by the term proportional to $\mathcal{R}_z \frac{k}{\eta}$ in the denominator of Eq. 21. This shows again that the higher order terms in the surface impedance cannot be neglected in the coupling impedance calculation for laminated structures.

III. CIRCULAR CHAMBER WITH LAMINATIONS

A. Wake functions

The momentum kick due to wake fields in circular chambers can be written as [17]

$$c\Delta p_z = \quad -qQW_0^{||}(z) \tag{92}$$

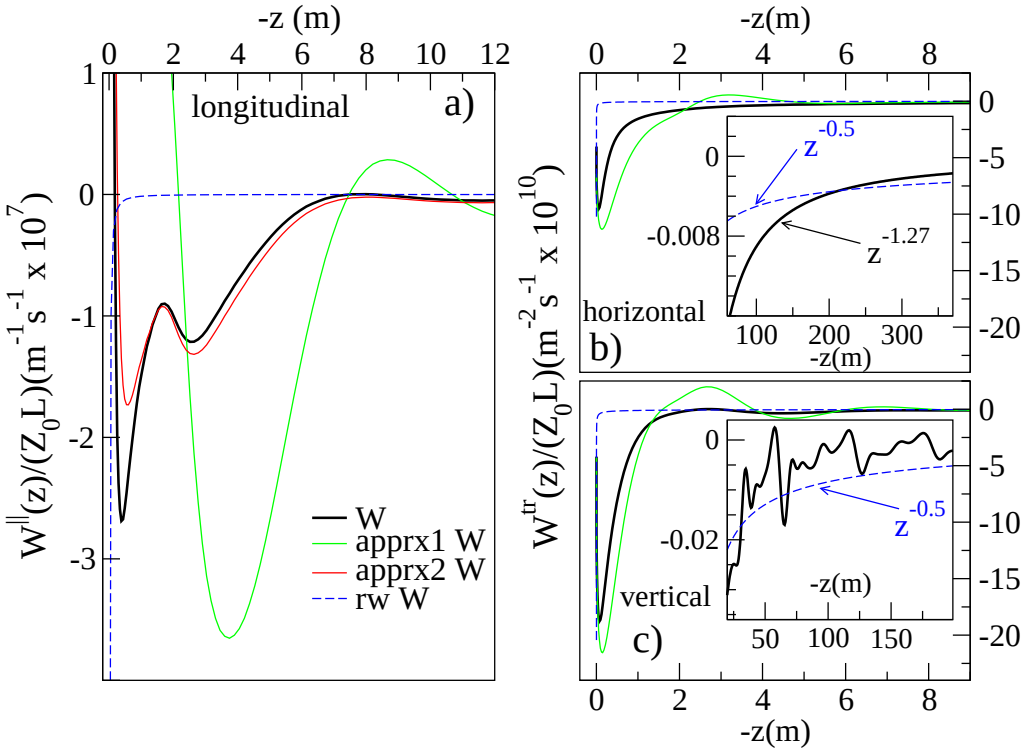

FIG. 5: Wake functions for a laminated chamber with parallel-plane geometry (black). The parameters are the same as in Fig. 4. a) Longitudinal wake function versus distance $|z|$. The wake is repulsive up to $|z| \approx 0.2m$, then becomes attractive with a maximum around $|z| \approx 0.4m$. The longitudinal wake is much larger than the resistive-wall case for an iron chamber (blue). The approximations which neglect the η-dependence of $\mathcal{R}_z$ (green) and the term proportional to $\mathcal{R}_z$ in the denominator of Eq. 19 (red) yield significantly different results. b and c) The horizontal (b) and vertical (c) wake functions. Compared to the resistive wall wake (blue) they are much larger at distance of order of meters. However they decays faster with increasing $|z|$. The horizontal wake becomes smaller than the resistive-wall wake at $|z| > 200m$, while the vertical one becomes smaller at $|z| > 30m$; see the inset. The neglect of the η-dependence of $\mathcal{R}_z$ (green) yields larger transverse wakes.

$$c\Delta p_x = -qQW_1^{\perp}(z)X \tag{93}$$
$$c\Delta p_y = -qQW_1^{\perp}(z)Y \tag{94}$$
$$\tag{95}$$

with (X, Y) representing the transverse displacement of the leading particle. The longitudinal wake, $W_0^{||}$, corresponds to the angular number $m = 0$ while the transverse wake, $W_1^{\perp}$, corresponds to $m = 1$. The wakes corresponding to higher values of m couple with higher-order terms in the beam displacement and are not considered here. Note that unlike the flat chamber, the term proportional to the trailing particle's displacement is not present in the transverse wake. The kicks along the x and y directions are described by the same function $W_1^{\perp}(z)$.

The wakes are Fourier transforms of the impedance functions, such that

$$W_0^{||}(z) = \frac{1}{2\pi}\int d\omega Z_0^{||}(\omega)e^{-j\frac{\omega}{c}z} \tag{96}$$
$$W_1^{\perp}(z) = \frac{j}{2\pi}\int d\omega Z_1^{\perp}(\omega)e^{-j\frac{\omega}{c}z} \ . \tag{97}$$

B. Impedance

As for the parallel-plane geometry, it is desirable to first derive equations which describe the coupling impedance as function of the surface impedance.

The Maxwell equations are solved in cylindrical coordinates. The charge and current decomposition are

$$\rho(r,\theta,z,t) = \sum_{m=0}^{\infty} \rho_m \delta(r-b) e^{j(\omega t - kz)} \tag{98}$$

$$\vec{J}(r,\theta,z,t) = \rho(r,\theta,z,t)\beta c\hat{z} \ , \tag{99}$$

where

$$\rho_m = \frac{I_m}{\pi b^{m+1}(1+\delta_{m0})} \ , \tag{100}$$

$$I_m = \rho b^m \ . \tag{101}$$

The field decomposition reads

$$(E_r(r,\theta), E_z(r,\theta), H_\theta(r,\theta)) = \sum_{m=0}^{\infty} (E_{rm}, E_{zm}, H_{\theta m}) \cos(m\theta) \tag{102}$$

$$(E_\theta(r,\theta), H_r(r,\theta), H_z(r,\theta)) = \sum_{m=0}^{\infty} (E_{\theta m}, H_{rm}, H_{zm}) \sin(m\theta) \tag{103}$$

$$\tag{104}$$

Note that for $m = 0$ the field components $E_\theta(r,\theta), H_r(r,\theta), H_z(r,\theta)$ are zero.

The solution of the electromagnetic field inside a round chamber has been calculated by numerous authors, see, e.g., Refs. [9, 17]. Inside the chamber, i.e. for $r < b$,

$$E_{z0} = A_0 \ , \tag{105}$$

for $m = 0$ and

$$E_{zm} = A_m r^m \tag{106}$$

$$Z_0 H_{zm} = -A_m r^m \ , \tag{107}$$

for $m \geq 1$.

The constants A_0 and A_m are determined from the boundary conditions at the pipe walls. They can also be expressed as functions of surface impedances

$$\mathcal{R}_{zm} = -\left.\frac{E_{zm}}{H_{\theta m}}\right|_{r=b} \tag{108}$$

$$\mathcal{R}_{\theta m} = \left.\frac{E_\theta}{H_{zm}}\right|_{r=b} \ . \tag{109}$$

with

$$A_0 = \frac{-\frac{\rho_1 \mathcal{R}_{z0}}{Z_0 2\pi\epsilon_0 b}}{1 + j\frac{\mathcal{R}_{z0}}{Z_0}\frac{kb}{2}}, \quad m = 0 \tag{110}$$

$$A_m = \frac{-\frac{I_m \mathcal{R}_{zm}}{Z_0 \pi\epsilon_0 b^{2m+1}}}{1 + j\frac{\mathcal{R}_{zm}}{Z_0}\left(\frac{kb}{m+1} - \frac{m}{bk}\right) + \frac{\mathcal{R}_{zm}\mathcal{R}_{\theta m}}{Z_0^2}}, \quad m \geq 1. \tag{111}$$

The longitudinal coupling impedance as function of surface impedance reads

$$Z_0^{||} = -\frac{E_z}{c\rho_1} = \frac{\frac{\mathcal{R}_{z0}}{2\pi b}}{1 + j\frac{\mathcal{R}_{z0}}{Z_0}\frac{kb}{2}}, \quad m = 0 \tag{112}$$

$$Z_m^{||} = -\frac{E_z}{cI_m r^m} = \frac{\frac{\mathcal{R}_{zm}}{\pi b^{2m+1}}}{1 + j\frac{\mathcal{R}_{zm}}{Z_0}\left(\frac{kb}{m+1} - \frac{m}{bk}\right) + \frac{\mathcal{R}_{zm}\mathcal{R}_{\theta m}}{Z_0^2}}, \quad m \geq 1, \tag{113}$$

while from Panofsy-Wenzel theorem the transverse impedance is

$$Z_m^{\perp} = \frac{c}{\omega} Z_m^{||} = \frac{\frac{c\mathcal{R}_{zm}}{\omega\pi b^{2m+1}}}{1 + j\frac{\mathcal{R}_{zm}}{Z_0}\left(\frac{kb}{m+1} - \frac{m}{bk}\right) + \frac{\mathcal{R}_{zm}\mathcal{R}_{\theta m}}{Z_0^2}}, \quad m \geq 1. \tag{114}$$

C. Resistive wall impedance

The equation for longitudinal field inside a cylindrical metallic pipe is

$$\frac{1}{r}\frac{\partial}{\partial r}(r\frac{\partial}{\partial r})\begin{pmatrix} E_z \\ H_z \end{pmatrix} = (\frac{m^2}{r} + \lambda_c^2 + p^2)\begin{pmatrix} E_z \\ H_z \end{pmatrix} \tag{115}$$

where $\lambda_c^2 = j\omega\sigma\mu = jkZ_0\sigma\mu_r$ and $p^2 = k^2(1-\epsilon_r\mu_r)$.

The transverse fields are derived from the longitudinal ones, see, e.g., Jackson[16].

We treat the $m = 0$ case first. The solution is

$$\begin{aligned} E_z &= A_0 \tfrac{K_0(\lambda r)}{K_0(\lambda b)} \\ E_r &= A_0 j \tfrac{k}{\lambda} \tfrac{K_0'(\lambda r)}{K_0(\lambda b)} \\ Z_0 H_\theta &= A_0 \tfrac{jk+Z_0\sigma}{\lambda} \tfrac{K_0'(\lambda r)}{K_0(\lambda b)} \end{aligned} \tag{116}$$

where $\lambda^2 = \lambda_c^2 + p^2$ and K_0 is the modified Bessel function of the second kind and order zero. It follows that

$$\frac{Z_0}{\mathcal{R}_{z0}} = -\frac{jk + Z_0\sigma}{\lambda}\frac{K_0'(\lambda b)}{K_0(\lambda b)} \ . \tag{117}$$

For $m \geq 1$

$$\begin{aligned} E_z &= -Z_0 H_z = A_m b^m \tfrac{K_m(\lambda r)}{K_m(\lambda b)} \\ E_r &= E_\theta = A_m b^m \tfrac{jk}{\lambda}(\tfrac{K_m'(\lambda r)}{K_m(\lambda b)} - \tfrac{m}{\lambda r}\tfrac{K_m(\lambda r)}{K_m(\lambda b)}) \\ Z_0 H_\theta &= A_m b^m (\tfrac{jk+Z_0\sigma}{\lambda}\tfrac{K_m'(\lambda r)}{K_m(\lambda b)} - \tfrac{jkm}{\lambda^2 r}\tfrac{K_m(\lambda r)}{K_m(\lambda b)}) \\ Z_0 H_r &= -A_m b^m (\tfrac{jk}{\lambda}\tfrac{K_m'(\lambda r)}{K_m(\lambda b)} - \tfrac{m}{\lambda r}\tfrac{jk+Z_0\sigma}{\lambda}\tfrac{K_m(\lambda r)}{K_m(\lambda b)}) \end{aligned} \tag{118}$$

where K_m is the modified Bessel function of second kind and of order m. One gets

$$\frac{Z_0}{\mathcal{R}_{zm}} = -\frac{jk + Z_0\sigma}{\lambda}\frac{K_m'(\lambda b)}{K_m(\lambda b)} + \frac{jkm}{\lambda^2 b} \ , \tag{119}$$

$$\frac{\mathcal{R}_{\theta m}}{Z_0} = -\frac{jk}{\lambda}\left(\frac{K_m'(\lambda b)}{K_m(\lambda b)} - \frac{m}{\lambda b}\right) \ . \tag{120}$$

Note that for the metallic round chamber, up to $\mathcal{O}(\sigma^{-1/2})$,

$$\mathcal{R}_{z0} \approx \mathcal{R}_{zm} \approx \mathcal{R}_{\theta m} \approx \frac{\lambda_c}{\sigma} \tag{121}$$

as is the case for the flat metallic chamber (see Eq. 31). In this approximation the surface impedance is independent of m. However, as we will see in Section III D, the m-dependence of the surface impedance is important in the calculation of the transverse impedance for a laminated circular chamber.

Since the surface impedance is small for metallic chambers, the terms proportional to it in the denominator of Eq.112, Eq.113 and Eq.114 can be neglected. The commonly used approximation for impedance in circular metallic pipes is

$$Z_0^{||} = \frac{\mathcal{R}_z}{2\pi b} \ , \tag{122}$$

$$Z_1^{\perp} = \frac{\mathcal{R}_z}{\pi k b^3} \ , \tag{123}$$

with $\mathcal{R}_z$ given by Eq. 121. Note that compared to the horizontal and the vertical impedances for the flat metallic chamber, Eq.36 and Eq.37, the circular transverse impedance is larger by factors of $\frac{24}{\pi^2}$ and $\frac{12}{\pi^2}$, respectively.

Another commonly encountered relation is given by

$$Z_1^{\perp} = \frac{2c}{\omega b^2} Z_0^{||} \ . \tag{124}$$

D. Laminated structures

Using the same justifications as for the flat chamber in Section II D, we have

$$\bar{\mathcal{R}}_z = \frac{\mathcal{R}_{1z}h + \mathcal{R}_{2z}\tau}{h+\tau} \tag{125}$$

and

$$\bar{\mathcal{R}}_\theta(\omega) \approx \mathcal{R}_{2\theta} \ . \tag{126}$$

where "1" denotes the crack region and "2" the region of the lamination.

1. *Surface impedance*

For large conductivity σ_2, the lamination surface impedances are given by

$$\mathcal{R}_{2zm} \approx \frac{1+j}{\delta_2\sigma_2} \ , \tag{127}$$

and

$$\mathcal{R}_{2\theta m} \approx \frac{1+j}{\delta_2\sigma_2}, \quad m \geq 1. \tag{128}$$

The next step is to calculate the crack surface impedance $\mathcal{R}_{1zm}$. As for the flat chamber, we assume that the field-dependence along the longitudinal direction is given by Eq. 50 and Eq. 51. Thus we have

$$(\frac{1}{r}\frac{\partial}{\partial r}(r\frac{\partial}{\partial r}) - \frac{m^2}{r} + q^2)\begin{pmatrix} E_z \\ H_z \end{pmatrix} = 0 \tag{129}$$

with $q^2 = \omega^2\epsilon_{1,2}\mu_{1,2} + g_{1,2}^2$.

Focusing on the $m = 0$ case first, the fields inside the crack are given by

$$E_z = A_1 \cosh(g_1 z)(H_0^{(2)}(qr) + \alpha H_0^{(1)}(qr)) \tag{130}$$

$$E_r = -A_1 \frac{g_1}{q} \sinh(g_1 z)(H_1^{(2)}(qr) + \alpha H_1^{(1)}(qr)) \tag{131}$$

$$Z_0 H_\theta = A_1 \frac{j\omega\epsilon_{1r}}{qc} \cosh(g_1 z)(H_1^{(2)}(qr) + \alpha H_1^{(1)}(qr)) \tag{132}$$

$$\tag{133}$$

where $H_n^{(1),(2)} = J_n \pm jY_n$ are Bessel functions of the third kind and order n. Inside the laminations

$$E_z = A_2 e^{-g_2|z|}(H_0^{(2)}(qr) + \alpha H_0^{(1)}(qr)) \tag{134}$$

$$E_r = A_2 e^{-g_2|z|} sgn(z) \frac{g_2}{q}(H_1^{(2)}(qr) + \alpha H_1^{(1)}(qr)) \tag{135}$$

$$Z_0 H_\theta = A_2 \frac{j\omega\epsilon_{2r}}{qc} e^{-g_2|z|}(H_1^{(2)}(qr) + \alpha H_1^{(1)}(qr)) \ . \tag{136}$$

$$\tag{137}$$

The condition $E_z|_{r=d} = 0$ implies

$$\alpha = -\frac{H_0^{(2)}(qd)}{H_0^{(1)}(qd)} \tag{138}$$

The continuity of the transverse fields at $z = \pm\frac{h}{2}$ requires $\omega^2\epsilon_1\mu_1 + g_1^2 = \omega^2\epsilon_2\mu_2 + g_2^2 = q^2$ and

$$g_1 \tanh(g_1 h/2) = -\frac{\epsilon_1}{\epsilon_2} g_2 \ . \tag{139}$$

This gives

$$g_1^2 = -\frac{2jg_2\epsilon_1\omega}{h\sigma_2} = (1-j)\omega^2\epsilon_1\mu_1\frac{\mu_2}{\mu_1}\frac{\delta}{h} \ , \tag{140}$$

where we assume $g_2 \approx \frac{1+j}{\delta_2} = \frac{(1+j)\sqrt{\omega\sigma_2\mu_2}}{\sqrt{2}}$, as for the flat chamber.

The crack surface impedance is

$$\frac{R_{1z0}}{Z_0} = j\frac{qc}{\omega\epsilon_{r1}}\frac{H_0^{(2)}(qb)H_0^{(1)}(qd) - H_0^{(1)}(qb)H_0^{(2)}(qd)}{H_1^{(2)}(qb)H_0^{(1)}(qd) - H_1^{(1)}(qb)H_0^{(2)}(qd)} \tag{141}$$

$$= j\frac{qc}{\omega\epsilon_{r1}}\frac{J_0(qb)Y_0(qd) - Y_0(qb)J_0(qd)}{J_1(qb)Y_0(qd) - Y_1(qb)J_0(qd)} \ . \tag{142}$$

This is the same result as in Ref [8, 9]. For $m \geq 1$ the fields in the crack are

$$E_z = A_1\cosh(g_1z)(H_m^{(2)}(qr) + \alpha H_m^{(1)}(qr))\cos(m\theta) \tag{143}$$

$$Z_0H_z = B_1\sinh(g_1z)(H_m^{(2)}(qr) + \beta H_m^{(1)}(qr))\sin(m\theta) \tag{144}$$

$$E_\theta = \left[-A_1\frac{g_1m}{q^2r}(H_m^{(2)}(qr) + \alpha H_m^{(1)}(qr)) + B_1\frac{jk\mu_{r1}}{q}(H'^{(2)}_m(qr) + \beta H'^{(1)}_m(qr)\right]\sinh(g_1z)\sin(m\theta) \tag{145}$$

$$Z_0H_\theta = \left[-A_1\frac{jk\epsilon_{r1}}{q}(H'^{(2)}_m(qr) + \alpha H'^{(1)}_m(qr)) + B_1\frac{g_1m}{q^2r}(H_m^{(2)}(qr) + \beta H_m^{(1)}(qr))\right]\cosh(g_1z)\sin(m\theta) \tag{146}$$

$$E_r = \left[A_1\frac{g_1}{q}(H'^{(2)}_m(qr) + \alpha H'^{(1)}_m(qr)) - B_1\frac{jkm\mu_{r1}}{q^2r}(H_m^{(2)}(qr) + \beta H_m^{(1)}(qr))\right]\sinh(g_1z)\cos(m\theta) \tag{147}$$

$$Z_0H_r = \left[-A_1\frac{jkm\epsilon_{r1}}{q^2r}(H_m^{(2)}(qr) + \alpha H_m^{(1)}(qr)) + B_1\frac{g_1}{q}(H'^{(2)}_m(qr) + \beta H'^{(1)}_m(qr))\right]\cosh(g_1z)\sin(m\theta) \ . \tag{148}$$

In the lamination we have

$$E_z = A_2e^{-g_2|z|}(H_m^{(2)}(qr) + \alpha H_m^{(1)}(qr))\cos(m\theta) \tag{149}$$

$$Z_0H_z = B_2e^{-g_2|z|}sgn(z)(H_m^{(2)}(qr) + \beta H_m^{(1)}(qr))\sin(m\theta) \tag{150}$$

$$E_\theta = \left[A_2\frac{g_2m}{q^2r}(H_m^{(2)}(qr) + \alpha H_m^{(1)}(qr)) + B_2\frac{jk\mu_{r2}}{q}(H'^{(2)}_m(qr) + \beta H'^{(1)}_m(qr))\right]e^{-g_2|z|}sgn(z)\sin(m\theta) \tag{151}$$

$$Z_0H_\theta = \left[-A_2\frac{jk\epsilon_{r2}}{q}(H'^{(2)}_m(qr) + \alpha H'^{(1)}_m(qr)) - B_2\frac{g_2m}{q^2r}(H_m^{(2)}(qr) + \beta H_m^{(1)}(qr))\right]e^{-g_2|z|}\sin(m\theta) \tag{152}$$

$$E_r = \left[-A_2\frac{g_2}{q}(H'^{(2)}_m(qr) + \alpha H'^{(1)}_m(qr)) - B_2\frac{jkm\mu_{r2}}{q^2r}(H_m^{(2)}(qr) + \beta H_m^{(1)}(qr))\right]e^{-g_2|z|}sgn(z)\cos(m\theta) \tag{153}$$

$$Z_0H_r = \left[-A_2\frac{jkm\epsilon_{r2}}{q^2r}(H_m^{(2)}(qr) + \alpha H_m^{(1)}(qr)) - B_2\frac{g_2}{q}(H'^{(2)}_m(qr) + \beta H'^{(1)}_m(qr))\right]e^{-g_2|z|}\sin(m\theta) \ . \tag{154}$$

As for the flat chamber, the condition for an acceptable solution is $B_1 = B_2 = 0$. $E_z = 0|_{r=d}$ implies $\alpha = -\frac{H_m^{(2)}(qd)}{H_m^{(1)}(qd)}$. The continuity of the transverse fields at $z = \pm\frac{h}{2}$ implies the same Eq.140 for g_1.

Consequently the crack surface impedance reads

$$\frac{\mathcal{R}_{1zm}}{Z_0} = -j\frac{qc}{\omega\epsilon_{r1}}\frac{H_m^{(2)}(qb)H_m^{(1)}(qd) - H_m^{(1)}(qb)H_m^{(2)}(qd)}{H'^{(2)}_m(qb)H_m^{(1)}(qd) - H'^{(1)}_m(qb)H_m^{(2)}(qd)} \tag{155}$$

$$= -j\frac{qc}{\omega\epsilon_{r1}}\frac{J_m(qb)Y_m(qd) - Y_m(qb)J_m(qd)}{J'_m(qb)Y_m(qd) - Y'_m(qb)J_m(qd)} \tag{156}$$

where

$$q^2 = \omega^2\epsilon_1\mu_1[(1 + (1-j)\frac{\mu_2}{\mu_1}\frac{\delta}{h}] \ . \tag{157}$$

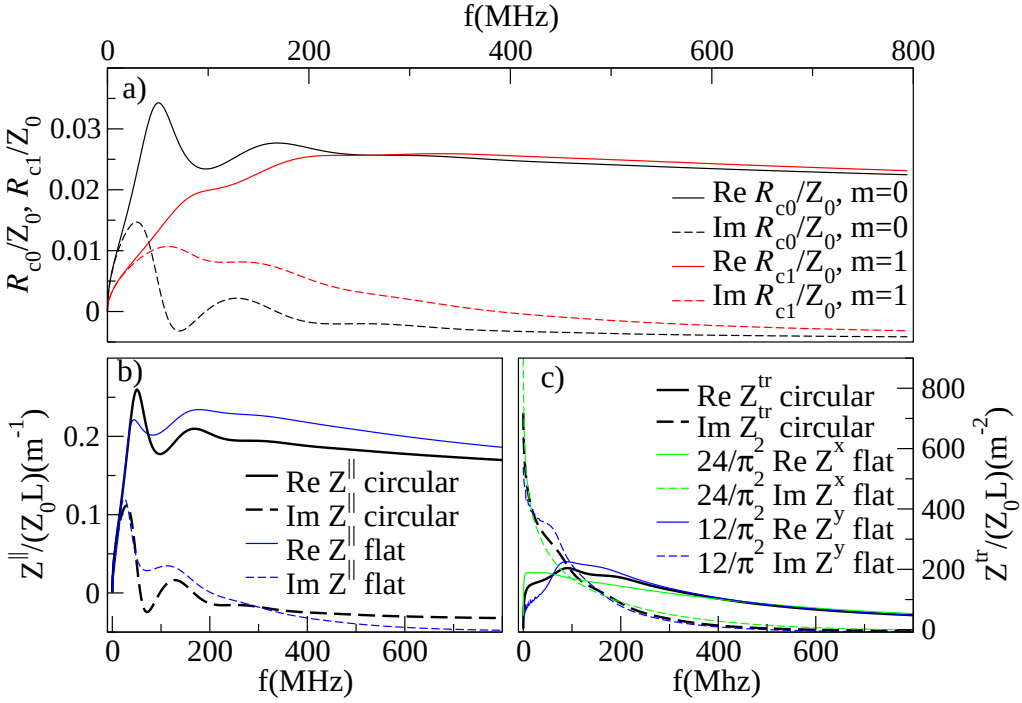

FIG. 6: The parameters for the round chamber with laminations are the same as for our flat chamber example, $b = 2.1cm$, $d = 15.24cm$, $h = 9.52 \times 10^{-4}cm$, $\tau = 6.35 \times 10^{-2}cm$, $\epsilon_{1r} = 4.75$, $\mu_{2r} = 100$, and $\sigma_2 = 0.5 \times 10^7(\Omega m)^{-1}$ a) Crack surface impedance for $m = 0$ (black) and $m = 1$ (red). At low frequency both cases display resistive-wall behavior proportional to $\sqrt{\omega}$. However while the $m = 0$ surface impedance is proportional to a factor of $\ln \frac{d}{b}$ the $m = 1$ one is proportional to a smaller factor of $\frac{d^2-b^2}{d^2+b^2}$. b) Longitudinal impedance ($m = 0$) for round chamber (black) and for flat chamber (blue). c) Transverse impedance for round chamber (black) and horizontal (vertical) impedance multiplied by $\frac{24}{\pi^2}$ (green) ($\frac{12}{\pi^2}$ (blue)) for flat chamber. Note the significant differences for frequencies smaller than $400MHz$.

2. *Coupling impedance for round chamber and comparison with flat chamber*

In Fig. 6a we show the crack surface impedance for angular numbers $m = 0$ and $m = 1$. Note that they are significantly different, thus producing different longitudinal wakes, unlike the resistive wall case. The low frequency behavior can be deduced by considering small-x approximations of the Bessel functions, $J_0(x) \approx 1$, $Y_0(x) \approx \frac{2}{\pi} \ln \frac{x}{2}$, $J_1(x) \approx \frac{1}{2}x$ and $Y_1(x) \approx -\frac{2}{\pi}\frac{1}{x}$. One gets

$$\mathcal{R}_{1z0} \approx j\frac{q^2}{\omega\epsilon_1} b \ln \frac{d}{b} \approx \frac{2}{h}\frac{1+j}{\delta_2\sigma_2} b \ln \frac{d}{b}, \quad m = 0 \tag{158}$$

and

$$\mathcal{R}_{1z1} \approx j\frac{q^2}{\omega\epsilon_1} b \frac{d^2-b^2}{d^2+b^2} \approx \frac{2}{h}\frac{1+j}{\delta_2\sigma_2} b \frac{d^2-b^2}{d^2+b^2}, \quad m = 1 \ . \tag{159}$$

Both $m = 0$ and $m = 1$ cases display resistive-wall like behavior at small frequencies, i.e. the surface impedance is proportional to $\sqrt{\omega}$. However the $m = 1$ surface impedance has a much smaller proportionality factor, $\frac{d^2-b^2}{d^2+b^2}$ compared to $\ln \frac{d}{b}$. In our example the resistive-wall behavior of the surface impedance can be observed up to $10 \sim 15MHz$.

Since the $m = 0$ and the $m = 1$ surface impedances are different, there is no simple relation such as Eq. 124 between the longitudinal $Z_0^{||}$ and the transverse $Z_1^{\perp}$ impedances.

In Figs. 6b and 6c a comparison between the circular chamber impedances and those corresponding to a flat chamber with the same parameters is shown. In the circular chamber case the longitudinal impedance has more strongly developed peaks around $40 \sim 50MHz$. For the comparison of the transverse impedances the flat chamber horizontal and vertical impedances are multiplied by the factors $\frac{24}{\pi^2}$ and $\frac{12}{\pi^2}$ respectively (see the discussion at the end of Section III C). Other significant differences in the transverse impedances of flat and round chambers can be noticed below $400MHz$.

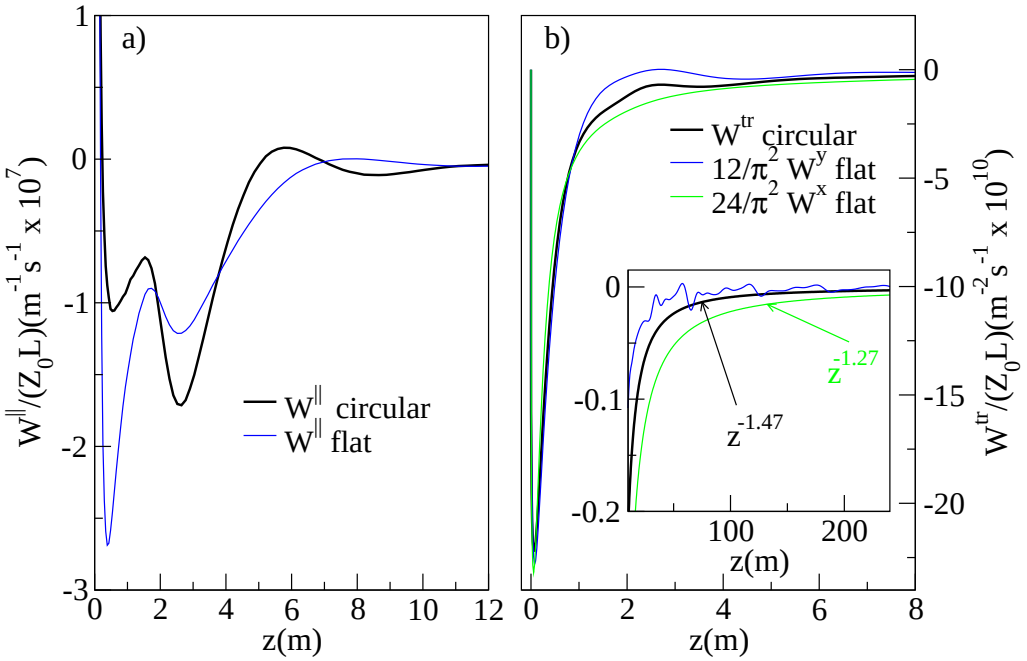

FIG. 7: Comparison between circular (black) laminated chamber and parallel-plane (blue) laminated chamber wake functions. a) Longitudinal wake. b) Transverse wake. The horizontal (green) (vertical (blue)) flat chambers wake is multiplied by a factor of $\frac{24}{\pi^2}$ ($\frac{12}{\pi^2}$). Inset: The long distance behavior of transverse wakes. In our example the wake for round chamber decays as $z^{-1.47}$ while the horizontal wake for flat chamber decays as $z^{-1.27}$.

3. Wake functions for round chamber and comparison with flat chamber

The wake functions for a round laminated chamber, obtained via Fourier transforms (Eq. 96 and Eq. 97) from the impedances shown in Fig. 6 are plotted in Fig. 7. For comparison the wake functions corresponding to a flat laminated chamber with the same parameters are also shown.

Fig. 7a displays the longitudinal wakes. Both circular (black) and flat (blue) longitudinal wakes are repulsive below $0.2m$ and attractive in the range $0.2m - 5m$. The flat chamber wake is larger around $0.4m$ while the round chamber one is more strongly peaked around $2.6m$. At $\approx 6m$ the round chamber longitudinal wake has a repulsive peak, becoming attractive again at $\approx 7m$, while the flat wake is smaller and attractive in this distance range. There is no significant difference between the longitudinal wakes at distances larger than $11m$. However, they are already small in this region.

The transverse wakes are shown in Fig. 7b. At distances of the order of a few meters, aside from the geometrically specific factors $\frac{24}{\pi^2}$ and $\frac{12}{\pi^2}$, the circular transverse wake is close to the horizontal and vertical parallel-plane wake. However, the asymptotic behavior at large distances is different, the circular wake going more rapidly to zero than the horizontal wake of the flat chamber. Since the horizontal wake plays a large role in the coherent tune shift in flat chambers [5], as we will discuss in Section IV, an approximation which uses the circular wake weighted by the geometric factor $\frac{\pi^2}{24}$ to describe the tune behavior in flat chambers would yield erroneous results.

IV. APPLICATION TO THE FERMILAB BOOSTER

About 60% of the Fermilab Booster synchrotron ring is made up of laminated iron magnets. There is no pipe in this region, the beam being directly exposed to the laminations. There are two types of combined function gradient magnets, focusing (F) and defocusing (D), with a geometry which in the first approximation can be considered parallel-plane[10]. The parameters of the F-magnets are given in the caption of Fig. 4 while the D-magnets have a slightly larger aperture $b = 2.9\ cm$. All the other parameters for the D-magnets are the same as those of the F-magnets.

The longitudinal impedance of Booster laminated magnets was measured by Crisp and Fellenz [3] using a stretched wire between the magnets ends. We find a good qualitative agreement between our calculation and their impedance, especially given the approximations used both in our calculations (such as the parallel-plane geometry for the gradient

magnets, non-frequency-dependent magnetic permeability in the laminations) and in their experiments (the wires disturb the electromagnetic fields inside the chamber). Compared to previous calculations using a simpler model [9], we notice a significant improvement, especially at frequencies below $200MHz$. For example, for the F-magnets (the impedance in Fig. 4a should be multiplied by $Z_0L = 1184m\Omega$), the real part of the longitudinal impedance shows a broad feature in the interval $100MHz - 200MHz$ with a maximum at $\sim 280\Omega$ similar to the measurements (see Fig.3 in Ref[3]). The imaginary part is inductive (positive) up to $200MHz$, as in the measurements; however, the calculation is about two times smaller than the measured result. At large frequencies there are still qualitative disagreements between the calculations and measurements, especially in the imaginary part of the longitudinal impedance. In our case it is capacitive (negative) while in the measurements it shows inductive behavior. However, both the positive measured value and our negative calculated value for the imaginary part of the longitudinal coupling impedance at large frequencies are small.

A measurable effect caused by the large impedance in Booster is the coherent tune shift which increases with the beam intensity. To calculate it we use the wake functions derived in Section III D 3 in a complex beam dynamics simulation which employs the Synergia code.

A. Synergia code and beam simulation

Synergia is an extensible beam dynamics framework utilizing state-of-the-art numerical libraries, solvers, and physics models. Synergia features 3D space charge solvers, impedance modules and arbitrary-order Lie maps for magnetic optics. A detailed description of Synergia can be found elsewhere [1, 2]. In order to model the Booster we developed new 3D space charge solvers suitable for parallel-plane and rectangular vacuum chambers for Synergia. We also developed new modules to simulate wake field effects based on the results presented in this paper.

In Synergia the beam is modeled as a large ($\approx 10^5 - 10^8$) set of macroparticles. When collective effects are turned off each particle propagates independently in the field created by the machine elements. The single-particle propagation is treated exactly using arbitrary-order maps. Collective effects are incorporated using the split operator method[18]. This implies a large number of momentum kicks during propagation. In brief, the simulation with collective effects is an interleaving sequence of single particle propagation followed by a momentum kick, followed by single particle propagation, followed by a momentum kick, etc... The error is $\mathcal{O}(\Delta s^3)$ where Δs is the distance between kicks. The number of kicks is taken to be large enough to reach convergence.

The wake kicks are implemented as follows. Each macroparticle "i" suffers a kick of its momentum proportional to

$$\Delta p_{zi} = \frac{-q^2}{c} \sum_{j>i} W^{||}(z_{ji}) \tag{160}$$

$$\Delta p_{xi} = \frac{-q^2}{c} \sum_{j>i} (W_x^{\perp}(z_{ji}) X_j - W_x^{\perp}(z_{ji}) x_i) \tag{161}$$

$$\Delta p_{yi} = \frac{-q^2}{c} \sum_{j>i} (W_y^{\perp}(z_{ji}) Y_j + W_x^{\perp}(z_{ji}) y_i) \ , \tag{162}$$

where the summation is over all the other particles "j" in front of the particle "i". The summation is not restricted only to the bunch "i" belongs to. The wake field created by all the other bunches as well as the effect of the previous turns are included in this summation.

The space charge solvers used in the simulations treat the vacuum chambers as ideal conductors. Thus image charges and image currents are always included in the space charge effects in our simulations. These effects are important since we present simulations at the Booster injection energy of 400 MeV ($\gamma = 1.42$), quite far from the relativistic limit. The space charge kicks are proportional to the electric field created by the other particles in the bunch. The field is calculated using particle in cell (PIC) Poisson solvers.

The Booster has 24 cells, each including F-magnets and D-magnets and circular pipe drift sections [4, 10]. We use different wake functions and space charge solvers for the F- and D-magnets. Circular space charge solvers are used for the drift sections.

The simulation is initialized with a six-dimensional Gaussian beam matched for propagation without collective effects. We run 84-bunch (full machine) simulations. The input parameters are $x_{rms} = 0.0086\ m$, $y_{rms} = 0.0032\ m$ and $z_{rms} = 0.88\ m$. Different beam intensities of up to 6×10^{10} particles per bunch are considered. These values are similar to those in the Booster during the experimental runs [10]. Since the experimental data was taken at the injection energy, in the simulations the phasing of the rf cavities is set up so that there is no net acceleration of the beam. To determine the coherent tunes, we measure the position of the beam center at different locations over 1000 turns. The tunes are extracted from the Fourier transform of the beam center displacement as a function of position.

B. Coherent tune shift and comparison with experiment

A simple inspection of the terms proportional to the trailing particle displacement in Eq. 2 and Eq. 3 (called *quadrupole*[5] or *detuning*[14] terms in the literature) reveal that they have different signs for the vertical and the horizontal directions. Keeping in mind that the wake function $W_x^{\perp}(z)$ is predominantly negative (see Fig. 5) it can be immediately deduced [5] that the effect of these terms will be to suppress the coherent vertical tune and increase the horizontal one. If the only collective effect acting on the beam were produced by these terms then one would expect the negative vertical tune shift to be equal to the positive horizontal tune shift. However, the terms proportional to the leading particle displacement as well as the space charge impedance effects act on suppressing both the vertical and the horizontal tunes. Thus they enhance the vertical tune suppression and compete with the horizontal tune enhancement produced by the quadrupole terms. This reasoning is corroborated by recent measurements [4] of the Booster coherent tunes which show a large decrease of the vertical tune and a small positive increase of the horizontal tune with increasing the beam intensity.

The data from the intensity-dependent tune scan shown in Fig. 8 were taken after the transverse Booster tunes had been separated to values of $\nu_x = 6.7$ (horizontal tune), and $\nu_y = 6.9$ (vertical tune). This was done by systematically changing the current settings of the quadrupole correction magnets using a method developed and described elsewhere [19]. The tunes were separated to better isolate tune shifts due to collective effects from the influence of machine-dependent mode mixing. Once the tunes were cleanly separated, the beam intensity was varied via injection, while all other machine parameters remained fixed. The tunes were obtained from turn-by-turn Fourier transforms of the 100 horizontal and vertical beam position monitors (BPMs) in the Booster, using an application developed to obtain beam frequency signatures with good signal to noise ratios [20]. In addition, a fast kicker was set to a periodic trigger to insure the betatron oscillations were large enough to allow a clear tune signature. The horizontal and vertical tunes were examined at 2 ms, 3 ms, and 5.5 ms, during the injection portion of the 33 ms Booster cycle. The injected beam intensity was varied from 0.9×10^{12} to 6.8×10^{12} protons.

A prior study was done where the tunes were not specifically decoupled, rather, they were highly coupled. It was uncertain how the machine coupling may have affected the evolution of the tunes, so the second study was done with the tunes separated. It was found that coupling effects in the first study were not significant, as the intensity-dependent tune shifts measured in both studies were quite similar [4]. The base machine tunes may be analogously controlled in the beam simulations. Simulations with different base tunes were performed and the results were in agreement with experimental measurements, the horizontal-vertical coupling did not play a significant role in the tune shift analysis.

In Figs. 8a and 8b, simulation of the coherent betatron tune shifts in the horizontal and vertical planes are compared with the experimental data [4]. Notice that the scale for the vertical tune shift is about 20 times larger than the scale for the horizontal tune shift. In order to better understand the contribution of the space charge and the coupling impedance several cases were studied. The red circles are the results of the simulations which include both space charge and coupling wake fields. The agreement with the experimental data is good. Estimating the measurement standard deviation σ_{meas}, we find our calculation to be within 3 σ_{meas} range. The vertical tunes are decreasing with intensity. As in the experiment, we find that the horizontal tunes do not change significantly with beam intensity, the slope being very small and positive. The green squares show the results when only the space charge interaction is taken into account. For the vertical case, both the wake and the space charge force decrease the tune, the coupling wake having a larger effect. For the horizontal case, the space charge force suppresses the tune, while the wake increases it. However, both effects are small.

V. CONCLUSIONS

We calculate the impedance and the wake functions for laminated structures with parallel-plane and circular geometries. First, the coupling impedance is derived as a function of the chamber surface impedance. Next, the surface impedance is calculated by solving the Maxwell equations inside the lamination and the crack regions. The impedance is evaluated on a large frequency range, the knowledge of both the small the large frequency behavior being necessary for the calculation of the wake functions.

We present a critical analysis of the resistive-wall impedance for metallic chambers and the approximations involved in its derivations. We show that the commonly used approximations, valid due to the small surface impedance associated with metallic pipes, do not hold for chambers with large surface impedance such as laminated structures. The truncation of the higher-order terms in the surface impedance cannot be done when calculating the impedance. While for the metallic chambers the dependence of the surface impedance on the horizontal wave number (in case of parallel-plane geometry) or on the angular number (in case of circular geometry) is not important, it is essential for the laminated chambers.

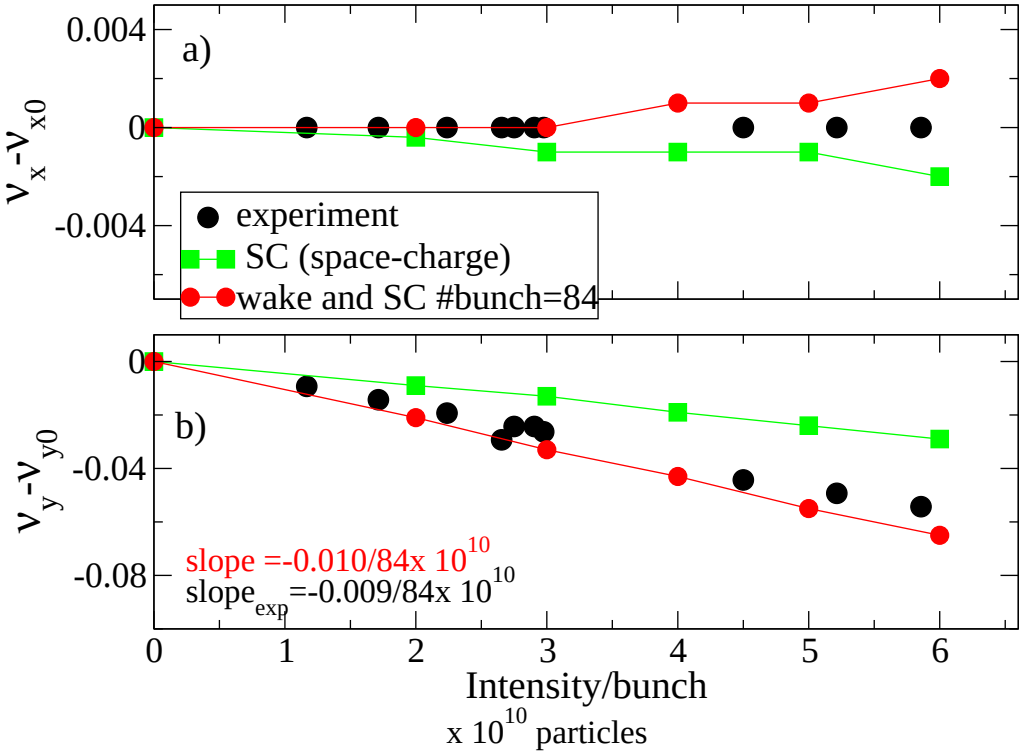

FIG. 8: Coherent horizontal (a) and vertical (b) tune shift versus beam intensity. The estimated tune uncertainty in calculations is less than 0.001. The vertical tune is suppressed while the horizontal tune changes very little. Space charge (SC) suppresses both the vertical and horizontal tunes, while the wake coupling suppresses the vertical tune and increases the horizontal tune. The calculation are in good agreement with the experiment, the deviation being within $3\sigma_{meas}$.

As an application, we calculate the coupling impedance and the wake functions for the Fermilab Booster magnets. The comparison of the longitudinal coupling impedance with the one measured by Crisp and Fellenz [3] gives better agreement than previous calculations.

We used the wake functions in realistic beam simulation using the Synergia code. New modules and subroutines were added to Synergia to take into account the wake interaction. We measured the beam coherent tune shift at injection energy and compare it with experiment [4]. We find that that the coherent vertical tune decreases with increasing beam intensity while the horizontal tune is almost constant, in good agreement with the measurements.

VI. ACKNOWLEDGMENTS

We thank Alexey Burov, Valeri Lebedev and K. Y. Ng for fruitful discussions. We also thank Yuri Alexahin, William Pellico, and William Marsh for help with beam studies. This work was supported by the United States Department of Energy under contract DE-AC02-07CH11359, the ComPASS project, funded through the Scientific Discovery through Advanced Computing program in the DOE Office of High Energy Physics, and NSF grant 0237162. This research used resources of the National Energy Research Scientific Computing Center, which is supported by the Office of Science of the U.S. Department of Energy under Contract No. DE-AC02-05CH11231, as well as resources of the Argonne Leadership Computing Facility at Argonne National Laboratory, which is supported by the Office of Science of the U.S. Department of Energy under contract DE-AC02-06CH11357.

[1] J. Amundson, P. Spentzouris, J. Qiang, R. Ryne, J. Comp. Phys. 211, 229 (2006).
[2] "Synergia2: A parallel framework for beam dynamics," *in preparation.*
[3] James L. Crisp and Brian Fellenz, Fermilab Report TM-2145 (2001).

[4] Daniel McCarron, Ph. D. Thesis, Fermilab, 2010.
[5] A. Chao, S. Heifets and Bruno Zotter, Phys. Rev. ST AB, 111001 (2002).
[6] S. C. Snowdon, Fermilab Report TM-277 (1970).
[7] A. G. Rugeira, Fermilab Report FN-220 (1971).
[8] R. Gluckstern, Fermilab Report TM-1374 (1985).
[9] K. Y. Ng, Fermilab Report FN-0744 (2004).
[10] Booster Rookie Book, Fermilab, `www-bdnew.fnal.gov/operations/rookie_books`.
[11] S. Heifets, A. Wagner, B. Zotter, SLAC/AP110 (1998).
[12] Not to be confused with the quadrupole terms corresponding to the angular number $m = 2$ in circular geometry, which are second order in the beam displacement.
[13] F. Zimmermann and K. Oide, PRST-AB, 044201 (2004).
[14] A. Burov and V. Lebedev, Proccedings of EPAC-2002, 1445 (2002).
[15] S. A. Heifets and S. A. Kheifets, Rev. of Mod. Phys. 63, 631 (1991).
[16] J. D. Jackson, Classical Electrodynamics, 3rd edition, John Wiley & Sons, Inc. New York (1999).
[17] A. Chao, "Physics of Collective Beam Instabilities in High Energy Accelerators," John Wiley & Sons, Inc. New York (1993).
[18] H. Yoshida, Phys. Lett. A 150, 262 (1990).
[19] Y.Alexahin, E. Gianfelice-Wendt, Fermilab-pub-06-093-AD (2006).
[20] Y.Alexahin, E. Gianfelice-Wendt, W. Marsh, IPAC-2010-MOPE084, Fermilab-conf-10-135-APC (2010).